

# Full-scale tests on masonry vaults strengthened with Steel Reinforced Grout

Stefano De Santis<sup>1\*</sup>, Francesca Roscini<sup>2</sup>, Gianmarco de Felice<sup>3</sup>

Roma Tre University, Department of Engineering. *Via Vito Volterra 62, 00146 Rome, Italy.*

<sup>1</sup> E: stefano.desantis@uniroma3.it. <sup>2</sup> E: francesca.roscini@uniroma3.it. <sup>3</sup> E: gianmarco.defelice@uniroma3.it.

\* Corresponding author. T: +39 06 5733 6387. F: +39 06 5733 3441.

## ABSTRACT

Masonry vaults can be particularly vulnerable against unsymmetrical service loads, support displacements and seismic actions. Retrofitting is often needed to ensure an adequate safety level according to current standard codes. Externally bonded composites are emerging as a possible retrofitting technique, but no experimental evidence is still available on the response of reinforced vaults reinforced taking into account the contribution of buttresses and backfill. This paper describes an experimental investigation on four full-scale vault specimens. One of them was tested unreinforced, whereas the other ones were strengthened with Steel Reinforced Grout (SRG), comprising ultra high tensile strength steel cords, bonded with lime-based mortar either to the extrados or to the intrados. The vaults were subjected to cyclic loading at 1/3 span. The backfill was visible through a panel of Plexiglas, allowing for the use of Digital Image Correlation to measure the displacement field and derive information on damage pattern and arch-fill interaction. Tests showed that SRG prevented the development of the four-hinge mechanism and avoided damage concentrations, increasing the deflection capacity and the strength of the arch by 2-3 times. Finally, it is shown that a simplified analytical approach based on limit analysis provides a reliable estimate of experimental load carrying capacity.

## Keywords

B. Strength; D. Mechanical testing; D. Surface analysis; Textile Reinforced Mortar (TRM).

## 1. INTRODUCTION

In many existing buildings all over the world, there are brick masonry vaults that either carry a floor or are simply a ceiling below the roof. They typically span some meters and their thickness ranges between 25cm (two brick heads) and 12cm (one brick head) or even 4-8cm. This latter typology of vaults, in which bricks are laid

lengthwise in one single leaf, or multiple leaves, are named timber vaults, Catalan vaults (they are widely used in Catalonia, but also in other Spanish regions, in Italy, etc.), or Guastavino vaults (from the name of the Spanish architect Guastavino who patented this arch style in the United States in 1885) [1]. Since their load carrying capacity mainly relies on the shape, the more slender vaults are particularly vulnerable against concentrated forces, unsymmetrical loads, support displacements and seismic actions. Therefore, retrofitting works are sometimes needed to ensure an adequate safety level according to current standard codes. To this purpose, externally bonded reinforcements with composite materials are particularly advantageous, since they provide high mechanical performances with minimum thickness and mass increase [2].

In masonry arched members, due to the lack of tensile strength, a failure mechanism activates by the formation of four hinges, alternated at the intrados and at the extrados. Composite reinforcements prevent the opening of cracks and, therefore, the onset of such collapse mechanism, avoid local falls of bricks, constrain the deflections of the vault and reduce the lateral thrust at the abutments [3]. In principle, the application of the strengthening system to one side only (either to the intrados or to the extrados) is sufficient to prevent the development of the hinges on this side and, therefore, the onset of the mechanism, whereas bonding the composite material to both surfaces is generally unnecessary. The intrados reinforcement is faster and cheaper than the extrados one, since the intrados surface is easily accessible from below. Its concave curvature may however reduce the adhesion of the composite, such that mechanical pins could be added. Many times, however, covering the lower surface of the vault is unfeasible since the paintings, the plaster or the fair face of the masonry have to be preserved. In this case, the strengthening system needs to be applied to the extrados. This requires that the flooring and the backfill are removed, which entails longer and more expensive work, but it can be easily combined with building side buttress walls or backings in solid brickwork over the abutments to constrain the deflection of the vault and with inserting tie-bars to prevent the relative movement of the side walls.

In the last decades, research activities and field applications have mainly used composites with polymeric matrix (Fibre Reinforced Polymers, FRPs) [4-8]. More recently composites with inorganic matrix, named Textile Reinforced Mortar (TRM), have also been applied [2,6]. TRMs consist of high strength fabrics (unidirectional textiles or bidirectional meshes) applied to the external surface of the structural members by means of cement or lime mortars. The use of inorganic matrices in place of organic ones provides better resistance at high temperatures, higher cost-efficiency, and the possibility of application to wet or irregular surfaces. TRMs with lime-based matrices also fulfil the preservation criteria required for applications to cultural heritage, as, with respect to cement mortars, they ensure a better physical/chemical compatibility with masonry substrates, vapour

permeability, and reversibility/removability (possibility of being removed with minimum damage to the substrate). On the other hand, the TRM-to-substrate bond strength may be lower than that of FRPs. The bond resisting mechanism of TRM systems is itself more complex, as failure may occur not only by cohesive debonding within the substrate (as with FRPs) but also by detachment within the thickness of the system or by textile sliding within the matrix [9].

TRMs have already been proposed to retrofit masonry arches making use of basalt [8,10-11], polyparaphenylene benzobisoxazole (PBO) [12-13], carbon [14], glass [15], and steel [6,8,16-17]. They have been applied either to the intrados of the arch [6,13,17], to its extrados [6,8,10,12-15,17], or to both surfaces [6,10]. In some cases, mechanical connectors have been used at the abutments to prevent end debonding [6], whereas in other studies the application of TRM systems has been combined with the construction of additional vault rings to increase the arch thickness (the *tabicada* technique) [15]. With respect to the unreinforced specimens, the ultimate load of strengthened arches increased by 3 to 20 times, and even more in case of application to both surfaces. The presence of the reinforcement modified the failure mode, since the activation of the four-hinge mechanism that typically occurred on unreinforced arches was replaced by a combination of reinforcement debonding, shear sliding and crushing of masonry, or tensile rupture of the textile. The deflection capacity also increased, in terms of both peak displacement and ductility, which resulted up to 10-15 times larger than those of unreinforced specimens, especially when steel or PBO textiles were used. Relatively lower enhancements were generally found on vaults reinforced with weaker textiles (e.g., glass or basalt) due to the brittle failure occurring by rupture of the fibres.

Despite the variability of the results, which is due to the different specimen geometry, material properties, experimental setups and TRM systems under investigation, these studies demonstrated the effectiveness of mortar-based composites for retrofitting masonry arches. The strength improvement achieved with TRMs also resulted comparable, or even higher, to that obtained with FRPs [6,8,16]. Nevertheless, the specimens tested so far were generally free-standing arches, i.e., backfill was not included. Only few works [11,16] took into account the influence of the buttresses. In [16], however, the buttresses were not built in contrast with a reaction structure, whereas in [11] only the vaults reinforced with TRM were provided with buttresses (that is, the retrofitting work included both the installation of the TRM and the construction of the buttresses). Finally, none of the specimens that have been tested so far were timber vaults, the most vulnerable vaulted structures. No experimental results are available on the gain in load carrying and deflection capacity that can be achieved with

mortar-based composites applied to timber vaults that are filled to carry a floor on top and provided with buttresses, even if this situation is often faced in retrofitting works.

This paper describes an experimental investigation performed in the laboratory on four vault specimens with 2.9m span, 65cm rise and 55mm thickness, provided with buttresses and backfill. One specimen was unreinforced and three were reinforced with Steel Reinforced Grout (SRG), comprising steel cords applied with lime-based mortar [18], with the aim of enhancing the load carrying capacity. With respect to the other fabrics used in TRM reinforcements, steel fabrics are unidirectional, are stiffer and stronger than glass and basalt, and thicker than carbon, aramid and PBO, are more durable in alkaline environment, and their shape provides a better interlocking within the mortar matrix [19]. To ensure durability, steel wires are coated with zinc to provide protection against salt attack and prevent rusting [20]. In this study, SRG was applied either to the extrados or to the intrados of the vault to investigate the different strengthening layouts that could be designed for structural applications in the field. Digital Image Correlation was used to measure displacements, which was possible thanks to the use of a Plexiglas spandrel panel that made the lateral surface of the specimen (arch barrel, buttresses, backfill) visible. A vertical load was applied over the backfill at 1/3 span and increased cyclically up to failure to investigate the increase in load carrying and deflection capacity provided by SRG and the modification of the associated damage pattern, failure mode, and arch-fill interaction. Finally, the load carrying capacity of the strengthened arches is estimated by limit analysis, using both a static and a kinematic approach.

## **2. EXPERIMENTAL SETUP**

### **2.1. Construction of the vault specimens**

Four full-scale vault specimens were built in the laboratory, using clay bricks (with 250mm×120mm×55mm size, 15.8kN/m<sup>3</sup> unit weight, 14.8N/mm<sup>2</sup> compressive strength, 2.5N/mm<sup>2</sup> tensile strength and 5.76kN/mm<sup>2</sup> Young's modulus [21]) and 10mm joints of lime mortar (5.2N/mm<sup>2</sup> compressive strength, 0.8N/mm<sup>2</sup> tensile strength and 1.5kN/mm<sup>2</sup> Young's modulus). The vaults had 2790mm span, 500mm width, 650mm rise. The bricks were laid lengthwise, i.e., on the shortest side, which resulted in a thickness of 55mm (Figure 1).

The experimental setup was designed to apply the most severe static loading condition that a vault can experience, that is, a concentrated load at 1/3 span [22], and the abutments were fixed. In the field, the relative support movements can be prevented by means of tie-bars [23].

First, 205mm high abutments (Figure 2a) were built in contrast with a reaction wall on one side and a stiff steel frame on the other side. Then, the arch barrel, made of 25 voussoirs, two entire bricks alternated with one brick and two half bricks, was built on wood forms (Figure 2b). Two buttresses, having 120mm thickness (one brick head), and 445mm height (seven layers), were built at each side (Figure 2c). The wood form was removed five days after the construction of the arch (Figure 2d). Two 20mm thick lateral panels, one of wood and one of Plexiglas, were placed on wood supports, and connected by 12  $\varnothing$ 8mm threaded bars to minimize out-of-plane deflections (Figure 2e). The backfill, consisting of 4÷8mm grain size gravel with 12.5kN/m<sup>3</sup> weight and  $\phi=39^\circ$  angle of internal friction, was set down manually (it was not densified mechanically), with a depth of 100mm in crown. Finally, a 20mm rubber mat was placed on top (Figure 2f).

## 2.2. Strengthening system and installation

### 2.2.1 Materials

The SRG systems used in this study comprise unidirectional textiles of Ultra High Tensile Strength Steel (UHTSS) cords (Figure 3a). Cords are made of five wires with 0.11mm<sup>2</sup> cross section area each, three rectilinear and two twisted around them, galvanized (coated with zinc) to provide protection against rusting. Two textiles were used, having either 8 cord/inch or 4 cord/inch density. The former has 3.18mm cord spacing, 0.168mm design thickness and 1200g/m<sup>2</sup> surface mass density (Figure 3b), whereas the latter has 6.35mm cord spacing, 0.084mm design thickness and 670g/m<sup>2</sup> surface mass density (Figure 3c). The steel textiles have 3186N/mm<sup>2</sup> tensile strength ( $f_t$ ), 184kN/mm<sup>2</sup> Young's modulus ( $E_t$ ) and 2.26% ultimate strain (from direct tensile tests [24]). To bond the steel textiles to the vault surface, a lime-based mortar was used, having grain size range of 0÷1.4mm, 20.6N/mm<sup>2</sup> compressive strength (from compression tests on cubic specimens), 11.4kN/mm<sup>2</sup> Young's modulus (from tests on cylinders), and 5.4N/mm<sup>2</sup> tensile strength (from three point bending tests). For the 4 cord/inch textile, the SRG-to-brickwork bond strength (axial stress in the textile at debonding) is  $f_b=2630\text{N/mm}^2$  on plane substrate [18], 2880N/mm<sup>2</sup> on convex surface with curvature radius of R=1800mm [23], and 1720N/mm<sup>2</sup> for convex surface with R=1800mm [25]; the effective transfer length has been estimated in the order of 200-250mm [9,18]. The SRG-to-brickwork bond strength of systems comprising 8 cord/inch textile is 647N/mm<sup>2</sup> on plane substrate, whilst no information is available on curved substrates.

The following specimens were tested:

- UNR: unreinforced;
- EX8: reinforced at the extrados with a 150mm wide strip of the 8 cord/in textile, with end connectors;

- EX4: reinforced at the extrados with a 150mm wide strip of the 4 cord/in textile, with end connectors;
- IN4: reinforced at the intrados with a 150mm wide strip of the 4 cord/in textile, with intermediate connectors;

The strengthening layouts were designed based on the different bond behaviour that SRG exhibits on curved surfaces. The textile with 8 cord/in, whose smaller spacing may reduce the textile-to-matrix bond strength, was used only for the extrados reinforcement, in which the curvature produces compressive normal stresses that improve the bond performance [23]. The 4 cord/in textile, instead, was used for both intrados and extrados reinforcements, because its larger cord spacing provides a better load transfer capacity, so it is suitable also for applications to concave surfaces in which tensile normal stresses take place at the reinforcement-to-substrate interface [25].

### 2.2.2 *Extrados strengthening*

Two specimens were reinforced at the extrados, one with the textile with 8 cords/in (EX8) and one with the textile with 4 cord/in (EX4). In both cases, a 150mm wide strip, corresponding to 48 or 24 cords, was bonded in the middle of the vault, and connected to the abutments by steel connectors to prevent end debonding. The cross section area of textile was  $A_f=25.6\text{mm}^2$  for EX8 and  $A_f=12.8\text{mm}^2$  for EX4. The strip was first cut to size and the connectors were prepared by rolling a 280mm long portion of textile. Resistive strain gauges were glued to record strains (Figure 4a). Then, the surface of the vault was cleaned with compressed air and wet with water. A first 5mm layer of mortar was laid down (Figure 4b). Then, the textile was placed by hand and pressed slightly, to make the fresh mortar pass through the voids between the cords (Figure 4c). A 5mm layer of mortar was applied on top (Figure 4d). The overall SRG thickness was about 10mm (Figure 4e). Clearly, especially in field applications, the thickness of the SRG strip may vary depending on the irregularities of the substrate.

Nevertheless, such variability is not expected to significantly affect the response of the reinforced structure, provided that it does not exceed 15-20mm [2,9]. Finally, the connectors were inserted in  $\varnothing 40\text{mm}$  holes drilled into the abutments (Figure 4f) and injected with a fluid lime-based grout. SRG was kept wet during the first seven days of curing and then left in standard laboratory conditions (20-22°C temperature and 50-60% relative humidity) for about one month before testing.

### 2.2.3 *Intrados strengthening*

One specimen, named IN4, was reinforced at the intrados with the 4 cord/in textile. As in EX4, the steel strip was 150mm wide and included 24 cords ( $A_f=12.8\text{mm}^2$ ). Due to the concave curvature of the substrate, which

induces tensile stresses at the SRG-to-masonry interface, seven connectors were included in the reinforcement at 500mm (4 voussoirs) spacing to improve adhesion. To this aim,  $\varnothing 30$ mm holes were drilled in the vault before installation (Figure 5a). Then, the intrados surface was cleaned and wet with water and the first 5mm layer of mortar matrix was laid down (Figure 5b). The textile, equipped with 20 strain gauges, was installed (Figure 5c). After the laying of the 5mm top layer of mortar, the steel connectors were inserted in the holes from below. Connectors consisted of a 100mm wide strip of steel textile, with a total length of 200mm, rolled in the initial 100mm upper portion and unfolded for the remaining 100mm lower portion (Figure 5d). They were fixed with a plastic wedge that kept their shape (Figure 5e). A fluid grout was injected from below (Figure 5f); it filled the voids between the connector and the masonry within the hole and protruded in the backfill over the extrados, in order to consolidate a small amount of gravel and prevent pull-out.

### **2.3. Instrumentation**

The load was applied at 1/3 span by means of an MTS 250kN hydraulic actuator, fixed to a reaction wall by a HEB270 steel cantilever (Figure 1), and recorded by an integrated load cell. Displacement controlled loading-unloading cycles were performed at 0.05mm/s (loading) and 0.20mm/s (unloading) rate, with increasing amplitude to failure. A 500mm long IPE240 steel bar was bolted to the head of the actuator to distribute the load over the width of the arch specimen and over a 120mm large portion of the rubber mat. The load spread through the gravel down to the vault extrados.

Four wire displacement transducers (WT) were installed on wood supports to measure the vertical displacement of two voussoirs, namely brick 17 (under the load, WT2 and WT4) and brick 10 (WT1 and WT3). Both the front (WT1 and WT2) and the back (WT3 and WT4) sides were monitored to detect possible undesired transversal mismatch. Two wire transducers (WT5 on the left and WT6 on the right) were installed to detect the movements of the abutments. Finally, two transducers were placed on the back wood panel (WT7) and on the front Plexiglas panel (WT8) to measure their out-of-plane deflection. For each of the three reinforced arches, 20 strain gauges were glued to the steel cords before SRG installation to measure the strain in the textile. Given the roughness of the cord surface, small plates of epoxy resin were realized to ensure the correct bond of the strain gauges. For each test, the positions of the strain gauges were selected based on the portions of reinforcement that were expected to undergo tensile stresses. In each of the selected positions, two strain gauges were installed and their average was taken as the strain in the textile in that point. Load, displacement and strain data were acquired at 10Hz sampling frequency.

In addition to these instruments, two-dimensional Digital Image Correlation (2D-DIC) was used to measure the displacements of the front side of the specimen. DIC is a full-field contactless optical method based on the correlation of the digital images taken during test execution, which provides the displacement field of the specimen surface [26]. To apply DIC, a speckle pattern, made of randomly distributed black dots on a white background, was realized on the masonry of the arch barrel and of the buttresses, and the backfill was made of white and black grains. The Plexiglas panel allowed the front side of the specimen (both the brickwork and the gravel) to be visible. Artificial markers (metal plates provided with the speckle pattern) were also placed on the IPE240 beam to record its displacement. DIC provided both the vertical and the horizontal displacements of the entire surface of the arch and of the buttresses, which would have been unfeasible with traditional devices, since an extremely large number of transducers would have been needed, with unsustainable efforts in terms of cost of equipment and test preparation [27]. DIC also detected crack occurrence (even before it was visible to the naked eye) [28] and provided information on displacements and strains in the backfill, similarly to what has been recently done on filled arch bridge models with Particle Image Velocimetry (PIV) [29]. During test execution, photographs were taken at 10s time interval with a Nikon D610 digital camera equipped with a lens with a focal length of 85mm. The camera was positioned on a stiff frame at 3.00m from the specimen. Pictures had 6016×4016 pixels, and one pixel had a size of 0.51mm. After the test, image processing made use of a biquintic B-splines sub-pixel interpolation scheme on the displacement field, which led to a resolution of less than 0.1mm and accuracy in the order of 0.1mm [26,30]. Errors related to radial lens distortion (caused by the optical distortion of the image in the zones at a larger distance from its centre) were corrected by the software [26] to improve accuracy. This latter was evaluated as the correlation error between two consecutive pictures taken before the beginning of the test with no load applied, and ranged between 0.11mm and 0.28mm, in the central and in the lateral zones of the specimen, respectively.

### **3. TEST RESULTS**

Aiming at showing the typical behaviour of a vault specimen (IN4 was selected as sake of example) and the actual constrain conditions provided by the experimental setup, the displacements measured by WT and DIC are represented against time in Figure 6. Downward displacements are assumed as positive, whereas upward displacements are assumed as negative.

First, no mismatch was detected between the displacements on the front and on the back sides of the arch barrel (WT1 vs. WT3 and WT2 vs. WT4, Figure 6a), indicating that no transversal uneven redistribution of the load or non-uniform response of the specimen took place. Secondly, the abutments (monitored by WT5 and WT6) resulted basically fixed, especially the right one, which was in contrast with the reaction wall. The maximum horizontal displacements were in the order of 1mm, and were mainly related to the compaction of the mortar joints and to small cracks developing during load cycles (Figure 6b). Finally, the agreement between the displacements recorded by wire transducers and DIC (Figures 6a,b) provides a validation of both measurement methods, despite the higher noise of DIC data for small displacements (of less than 1mm). The wood and Plexiglas panels (monitored by WT7 and WT8, respectively) provided a stiff constrain to the fill soil even if their out-of-plane displacements were not completely negligible (up to 1.4mm), especially in the final part of the test (Figure 6c).

The first unloading-reloading cycles were performed at 1kN interval (i.e., load was reduced when 1kN, 2kN, etc. were attained). These cycles mainly compacted the backfill without producing significant deflections of the arch barrel. Additionally, the residual displacements at the end of the unloading cycles were mainly related to such compaction of the gravel rather than to irreversible deflections of the vault, with the only exception of the last cycles (Figure 6d).

Test results are described and commented hereafter. The load-displacement response curves are shown in Figure 7, having the load on the y-axis and the vertical displacements of bricks 17 and 10 on the x-axis. As before, downwards displacements, as well as the load, are assumed as positive, whereas upwards displacement are assumed as negative. Figures 8-11 show the crack pattern and the failure modes of the tested specimens; Figures 9-11 also show the strain profiles in the steel textile, plotted for selected steps of the test identified by letters A-H and associated to progressive values of displacement of brick 17 (s) and of applied load (F). The strain profiles are not represented in the region where the SRG is compressed and does not provide any contributions. The damage patterns of the reinforced vaults are collected in Figure 12. The deformed configurations measured by DIC at peak and at collapse of the axis of the vault and of the top surface of the backfill are shown in Figure 13. Finally, the fields of vertical displacements (on which the self-weight and the external load spend work) recorded by DIC on the entire lateral specimen surface are shown in Figures 14 (at peak load) and 15 (at collapse) together with the arrows of total displacements.

Main results are collected in Table 1, in which  $F_{\max}$  is the maximum load and  $\Delta F_{\max}$  is its ratio with respect to that of the unreinforced vault,  $s(F_{\max})^+$  and  $s(F_{\max})^-$  are the displacements corresponding to  $F_{\max}$  of bricks 17 and

10, respectively, and  $s_u^+$  and  $s_u^-$  are their ultimate displacements (at failure). Finally,  $\epsilon_{\max}$  is the maximum strain measured on the textile,  $\sigma_{\max}$  is the stress estimated as  $\sigma_{\max} = \epsilon_{\max} \cdot E_f$  (considering that the stiffening effect of the lime mortar matrix is negligible after cracking and that the steel cords exhibit a non-linear response only when the stress is close to the tensile strength [18,24]),  $\eta_t$  is the exploitation ratio of the tensile strength of the textile calculated as  $\eta_t = \sigma_{\max} / f_t$ , whereas  $\eta_b = \sigma_{\max} / f_b$  is referred to its bond strength on plane substrate.

### 3.1. Unreinforced vault

In the unreinforced arch (UNR), after the initial cycles that compacted the backfill, cracks appeared on the arch barrel after a load of 4kN was overstepped. This produced a reduction of the stiffness with the development of the first non-negligible vault deflections. A four-hinge mechanism developed, with hinges between bricks 6-7 (crack at the intrados), 11-12 (extrados), 16-17 (intrados, below the load), and 20-21 (extrados), as shown in Figure 8. The hinges in the central region of the arch (11-12 and 16-17) appeared before the peak load, whereas the other ones developed in the post-peak phase. The maximum load was 5.9kN. Then, a post-peak phase took place during which the load carrying capacity decreased linearly. At the end of the test, the displacement of brick 17 was  $s(F_{\max})^+ = 36.1\text{mm}$  (downwards), whereas that of brick 10 was  $s(F_{\max})^- = -38.1\text{mm}$  (upwards). The buttress walls reduced the real span of the arch, especially on its left side, whose upward movement was constrained. On the other side, a crack developed between the extrados of the arch and the buttress, which, therefore, had a negligible influence on the response of the vault since its right portion moved downwards.

It is worth noting that the load carrying capacity of the vault without backfill, estimated using a limit analysis approach, is 0.6kN if buttresses are neglected, 1.8kN if buttresses (but no backfill) are included, or, finally, 3.4kN if the self-weight and the load spreading effect of the backfill are considered but the contribution of this latter to the resistance (related to the passive pressures associated to vault upward deflections) is neglected.

### 3.2. Vaults reinforced at the extrados

The vault reinforced with the 8 cord/in textile at the extrados (EX8) attained a maximum load of 15.9kN (+174% with respect to UNR). The SRG limited the opening of cracks at the extrados and the upward deflection of the arch, whereas a crack developed at the intrados between bricks 16-17 (below the load) and between bricks 5-6, also involving the left buttress wall (Figure 9). When approaching the maximum load, detachment activated at the textile-to-matrix interface, cracks appeared also at the extrados between bricks 12-13 (Figure 12b) and between brick 25 and the right abutment. With respect to UNR, the failure mechanism involved a larger portion

of arch barrel, and the four hinges were associated to a shear sliding between bricks 16-17 (Figure 12a) and to a significant crushing of the masonry. Apart from the compressed edges of the bricks at the hinges, a longitudinal crack also appeared in the middle of the arch barrel (Figure 12c), indicating that the reinforcement led to the attainment of a high bending moment, associated to high compressive stresses. At collapse, the vault detached from the right buttress, which was also involved in the failure mode, as it separated from the abutment and rotated around the springing section. Since the SRG was not visible during test execution, progressive damage development could not be detected. After the end of the test, the backfill was removed and the final damage pattern was surveyed. Detachment took place at the textile-to-matrix interface where the extrados was compressed, thus appearing mainly due to instability rather than to shear. On the other hand, the development of cracks at the extrados indicated that some sliding had occurred between the cords and the mortar, reducing the effectiveness of the reinforcement.

The stiffness of the reinforced arch in the very first phase of the test (load lower than 4kN) was basically the same of UNR, since the SRG was not involved in the response, as revealed by the negligible strain recorded on the cords (see the profile at stage A in Figure 9). Then, the load was transferred to the reinforcement between bricks 9 and 15 and between 21 and 25, where it was subjected to tensile stresses to constrain the opening of cracks at the extrados. This resulted in a stiffer behavior than UNR (Figure 7). Moreover, the SRG entailed a higher peak deflection,  $s(F_{\max})^+$  being ten times larger. Accordingly, the displacement field recorded by DIC in the backfill indicated that, with respect to UNR, a larger volume of backfill was mobilized above the extrados surface of the vault that moved upwards (Figures 14a,b). Finally, at collapse, the extrados reinforcement allowed for a more distributed deflection of the left portion of the vault, moving upwards (note that the values of  $s_u^-$  are similar), whereas much larger displacements were recorded under the load ( $s_u^+$ ) due to the concentration of rotation at the intrados hinge (between bricks 16 and 17).

The strain in the steel cords at the attainment of the peak load (stage E) was  $2.8 \times 10^{-3}$  (corresponding to a stress of about 515N/mm<sup>2</sup>) and was recorded by the strain gauges placed over brick 11 (Figure 9), whereas the maximum strain value was  $\epsilon_{\max} = 6.7 \times 10^{-3}$ , corresponding to an estimated stress  $\sigma_{\max} = 1230\text{N/mm}^2$ , which is 38.7% of its tensile strength and nearly twice its bond strength (the increase may be attributed both to the convex surface as well as to the longer bond length [23]). Such strain level was reached at brick 11 in the first part of the post-peak phase (stages F and G). Then, it partially reduced to  $5 \times 10^{-3}$  (stage H) when the strain redistributed over a longer portion of SRG (between bricks 9 and 15). The most stressed portion of SRG was far enough from the left abutment that the load was effectively transferred by SRG-to-substrate adhesion and the connector

remained unused. It should also be considered that, in this region, the extrados of the vault was compressed and its upward movement was constrained by the buttress. The connector on the right abutment, instead, was involved in the response of the vault, especially when approaching failure, after the SRG had already detached from the masonry substrate. No pull-out failure however occurred.

EX4 specimen (reinforced at the extrados with the 4 cord/in textile) attained a maximum load of  $F_{\max}=11.7\text{kN}$  (+102%), with a displacement of brick 17 of  $s(F_{\max})^+=15.8\text{mm}$  (Figure 7). Failure occurred by shear sliding between bricks 16-17 and 17-18 (Figure 12d), at  $s_u^+=73.9\text{mm}$ . Cracks also appeared at the intrados between bricks 5-6, at the extrados between bricks 11-12 and 13-14, and, finally, at the extrados between brick 25 and the right abutment, with a detachment from the buttress (Figure 10). The position of the hinges was analogous to EX8. In EX4, however, no detachments were detected in the SRG (thanks to the better textile-to-matrix interlocking of the 4 cord/in textile with respect to the denser 8 cord/in one), apart from where shear failure took place and over bricks 6-8, which was probably related to a local dip of the vault surface (Figure 12e). A longitudinal crack developed (Figure 12f), but if it was narrower than in EX8, due to the lower applied load. The lower load carrying capacity with respect to EX8 may be attributed to the larger deformability of the SRG (which did not constrain the arch deflections with the same effectiveness), but also to local imperfections or initial misalignments of the bricks in the arch barrel below the load, where shear sliding occurred.

The displacement capacity of EX4 was similar to that of EX8, with an even slightly larger ultimate upward displacement ( $s_u^-$ ), associated to a less steep post-peak branch, due to the lower axial stiffness of the reinforcement (Figure 7). Indeed, the deformed configurations at peak and at collapse show only slightly larger displacements of the entire left portion of the vault (moving upwards, Figures 13c,d, 14c,d and 15c,d). The displacements measured by DIC indicate that these larger displacements were associated to a higher concentration in the backfill over the extrados on the left side (Figures 14c and 15c).

Like EX8, the portion of SRG that was significantly involved in the response was comprised between bricks 9 and 15, even if, in this case, strains mainly concentrated at brick 13, and near the left abutment (Figure 10). Since the load was lower than in EX8, however, the strain at peak load (stage C) was  $1.8\times 10^{-3}$  (corresponding to a stress of  $330\text{N/mm}^2$ ) at brick 13, whereas the maximum strain was  $\varepsilon_{\max}=2.5\times 10^{-3}$  ( $\sigma_{\max}=460\text{N/mm}^2$ ,  $\eta_t=14.4\%$ ,  $\eta_b=17.5\%$ ). The connector on the right abutment reached a strain of  $1.8\times 10^{-3}$  at stage H (end of the post-peak phase, close to collapse) indicating that it contributed to the behaviour of the reinforcement system, but it was not pulled out. Finally, on the left portion of SRG, the strains were basically null.

### 3.3. Vault reinforced at the intrados

The maximum load exhibited by the arch reinforced with the 4 cord/in textile at the intrados (IN4) was 16.2kN (+179%). The downward displacement of brick 17 at the peak  $s(F_{\max})^+$  was lower than in EX8 and EX4 (Figure 7), due to the presence of the SRG at the intrados. This was not associated to an increase of the peak upward displacement of brick 10  $s(F_{\max})^-$ , even if no reinforcements were bonded to the extrados. At the attainment of the peak load, SRG detached at the textile-to-matrix interface between the connectors in the whole central portion of the arch barrel, due to the tensile normal stresses caused by the concave curvature of the substrate. Since the connectors did not pull out, the textile still worked as an unbonded tendon in this region and contributed to the load carrying capacity of the arch in the post-peak phase (Figure 12g). Between the left abutment and brick 8, instead, the SRG effectively prevented the opening of a crack at the intrados (Figure 12h). The steel cords experienced a strain of  $1.1 \times 10^{-3}$  (200N/mm<sup>2</sup>) at peak load (stage D) and of  $\varepsilon_{\max}=3.7 \times 10^{-3}$  ( $\sigma_{\max}=681\text{N/mm}^2$ ,  $\eta_t=21.4\%$ ,  $\eta_b=25.9\%$ ) at collapse (stage H), with a progressive increase between bricks 2-6, whereas a sudden strain growth was recorded at brick 8 in the very last part of the test (Figure 11). The SRG detachment from the substrate made the readings of the strain gauges unreliable between bricks 14-20 in the post-peak phase (stages from E to H).

None of the steel connectors was pulled out, indicating an effective anchorage in the arch section and in the backfill consolidated by the grout injection. Nevertheless, those in the middle of the arch (which experienced the highest stresses) were unfolded and their wedge was partially expelled, which compromised their effectiveness and led to a faster decrease of the post-peak strength with respect to the arches reinforced at the extrados. The ultimate displacements ( $s_u^+$  and  $s_u^-$ ) were slightly larger than in EX8 and EX4, but were associated to much lower load values.

After the detachment of SRG, hinges developed between bricks 6-7 (intrados), 10-11 (extrados), 16-17 (at the intrados, below the load), and 21-22 (extrados, with detachment from the buttress wall), as shown in Figures 11 and 12i. The masonry locally cracked where the hinges formed. The left buttress also cracked and detached from both the arch barrel and the abutment, but it was not directly involved in the collapse mechanism. Cracks in the buttress mainly developed during the unloading cycles due to its lower capacity of following the downwards deflection of the underlying vault that took place when the load decreased.

Both the deformed configurations and the displacement fields indicate that the intrados reinforcement entailed a more distributed downward deflection of the right portion of the vault (Figures 12e,f), whereas it did not prevent the localization of backfill mobilization on the other side, where a crack developed at the extrados and the arch

barrel (Figure 14g). The comparison between EX4 and IN4 specimens, in which SRG had the same axial stiffness, indicates that the intrados reinforcement entailed a stiffer behaviour of the vault when subjected to vertical loads.

Thanks to the use of the Plexiglass panel, the backfill was visible and the displacement fields were measured by DIC. This provided information on the volume of gravel that was mobilized in the tests and on arch-fill interaction. Some differences are clearly identifiable between the unreinforced vault and the reinforced ones. SRG entailed the involvement of a much larger volume of backfill, both on the left side (moving upwards) and on the right side (moving downwards). Furthermore, at peak load (Figure 14), when the displacement fields were mainly related to the load distribution, the inclination of the boundary lines that identify the volume of mobilized backfill was 36-37° in UNR and 42-43° in the other specimens. As a result, the portion of arch barrel involved in the response was larger in reinforced vaults (between bricks 15 and 18) than in the unreinforced ones (bricks 14-21).

At failure (Figure 15), the displacement fields, mainly related to the collapse mechanism (i.e., to the position of the hinges), indicate that in IN4 (Figure 15d) a larger volume of backfill was mobilized below the load with respect to the other specimens, thanks to the broader distribution of downwards displacement provided to the arch barrel by the intrados SRG. On the left side, instead, a localization of displacement was detected in IN4 (Figure 15d). Such concentration was found also in UNR (Figure 15a) but not in EX8 (Figure 15b) and EX4 (Figure 15c) in which the extrados SRG entailed a broader distribution of the load transferred to the backfill by the arch barrel moving upwards.

#### **4. ANALYTICAL ESTIMATE OF THE LOAD CARRYING CAPACITY**

In this section, the load carrying capacity ( $F_{max}$ ) of the reinforced arch specimens EX8 and IN4 is estimated with a simplified analytical method based on limit analysis. EX4 is excluded because shear failure is not predicted by this approach. Some attempts of applying limit analysis to masonry arches reinforced with externally bonded FRP [31-32] or TRM [12] composites have already been made using the upper bound theorem (that is, by adopting a kinematic approach). The failure mode (defined by the position of the hinges) is determined numerically by solving a minimization problem within linear [31-32] or nonlinear [33] programming schemes. In this work, with the aim of contributing to the development of simplified methods suitable for engineering

design purposes, both a static approach and a kinematic approach are used, starting from the collapse mechanism observed in the experimental tests and identified by the position of the four hinges, as shown in Figure 16.

Masonry is assumed to have no tensile strength and infinite friction angle. For SRG, the maximum attainable load  $F_s$  assumed in the analysis is the product of the tensile strength  $f_t=3186\text{kN/mm}^2$  and the cross section area of the textile, which results in  $F_s=81.6\text{kN}$  for EX8 ( $A_t=25.6\text{mm}^2$ ) and  $F_s=40.8\text{kN}$  for IN4 ( $A_t=12.8\text{mm}^2$ ). Finally, as for the backfill, the self-weight and the load spreading effect (depending on the angle of internal friction  $\phi=39^\circ$ ) are considered, but passive pressures are neglected.

In the static approach, the axial force (N) - bending moment (M) strength domain of the cross section is built for the vault reinforced at the extrados (Figure 17a) and at the intrados (Figure 17b). A compressive strength of the masonry of  $8\text{N/mm}^2$  is considered and it is assumed that failure is attained at the same time in the masonry and in the SRG. In the arch reinforced at the extrados, starting from the position of the hinges provided by experiments (Figure 16a), equilibrium is obtained requiring that the stress resultant in sections 1 and 3 (see Figure 17a) is applied at the hinges. The maximum statically and plastically admissible load  $F_{\max}$  is then obtained by imposing that in sections 2 and 4, the N,M stress state falls on the boundary of the domain. According to this approach, the balance and strength conditions are established only at the hinge sections. The static approach provides an estimated  $F_{\max}$  of  $14.0\text{kN}$  (-12% with respect to the experimental value). In a similar manner, for the arch reinforced at the intrados (figure 16b), the maximum load that is in equilibrium and satisfies the strength condition in Figure 17b is equal to  $14.1\text{kN}$ , which is 13% lower than the experimental value.

In the kinematic approach, the collapse mechanism provided by the experiments is considered as shown in Figure 16, for either the reinforcement at the extrados or at the intrados, resulting in the vertical component (v) of the displacement field as depicted in the figure. It is assumed that the masonry is rigid and, for the sake of simplicity, that it has infinite compressive strength, which yields that the hinges develop at the edge of the cross section. Collapse occurs when the work spent by the external loads (self-weight of vault and backfill, and external load F) in the displacement field (v) equals the maximum resisting work given by the tensile load  $F_s$  in SRG at hinges 2 and 4 in the arch reinforced at the extrados and at hinges 1 and 3 in that reinforced at the intrados.  $F_s$  spends work in the relative displacement associated with the hinge opening, which is given by  $t\cdot\theta$ , t being the thickness of the vault and  $\theta$  the relative rotation of the two portions separated by the hinge. By using the kinematic approach, the estimated  $F_{\max}$  is  $17.8\text{kN}$  for the arch reinforced at the extrados (+12% with respect to the experimental value) and  $18.5\text{kN}$  for that reinforced at the intrados (+14%).

Both limit analysis approaches provide a reliable estimate of the load carrying capacity, thus appearing suitable for an expeditious assessment of the vault strengthened with externally bonded TRM/SRG and for a preliminary reinforcement design. However, the simplifying assumptions may result in a reduction of the accuracy, especially in the kinematic approach, for which the error is not on the safe side. Finally, differently from the present case, the position of the plastic hinges is generally unknown a priori and needs to be either assumed based on experience or determined as that associated to the lowest value of the external load.

## CONCLUSIONS

An experimental investigation was carried out on full-scale masonry vaults, provided with buttresses and backfill, subjected to a cyclic load at 1/3 span. The specimens were strengthened with Steel Reinforced Grout, either to the extrados or to the intrados. Two textiles were used for extrados reinforcements, having density of either 8 cord/inch or 4 cord/inch. The former solution provided an increase of load carrying capacity of 174% with respect to the unreinforced specimen. Collapse occurred by a combination of crushing and shear sliding of brickwork and debonding of the reinforcement at the textile-to-matrix interface. SRG with the 4 cord/inch textile led to a relatively lower gain in strength (+102%), due to its higher deformability, which entailed larger deflections of the arch barrel up to the occurrence of a shear failure. The exploitation of the textile was lower than in the previous case, even if the lower cord density provided a better bond behaviour that prevented detachments. In extrados reinforcements, steel connectors effectively prevented end debonding at the abutments. The intrados reinforcement was realized with the 4 cord/inch textile. In this case, the load carrying capacity of the vault was increased by 179%. The textile debonded from the substrate, due to the concavity of the intrados, between intermediate connectors (500mm spaced), which effectively prevented the complete SRG detachment. With respect to the unreinforced specimen, all SRG systems limited the opening of cracks on their side (either extrados or intrados) and the activation of the four-hinge mechanism, avoided displacement concentrations and entailed a larger volume of mobilized backfill. Accordingly, the displacement capacity was improved in terms of both peak displacement (increased by 4-10 times) and ultimate displacement (up to two times). Test outcomes clearly demonstrate the effectiveness of SRG for increasing the load carrying capacity of masonry vaults, and the important role played by the connectors, to be placed either at the abutments (extrados applications) or along the arch barrel (intrados applications). With respect to other studies on masonry arches retrofitted with TRMs, however, the gain in strength over unreinforced specimens was relatively lower. On the

one hand, this is due to the presence of buttresses and backfill, which significantly contributed to the capacity of the vault, especially without reinforcement. On the other hand, the possible increase of strength appears limited by the slenderness. Thin vaults retrofitted with stiff strengthening systems may fail by crushing due to the concentration of compressive stresses in the sections subjected to the highest bending moment. Vaults retrofitted with more deformable reinforcements, which allow for larger deflections, may instead fail by sliding due to the concentration of shear stresses. Clearly, the possible occurrence of shear failure may be caused also by reduced friction and cohesion or relatively low axial load at the joints, and was observed especially in flat arches [10-11,34].

The condition of fixed abutments assumed in this study cannot always be attained in practice, and therefore more investigations are needed to analyse the support displacement capacity of masonry vaults reinforced with externally bonded TRM/SRG composites. Furthermore, experimental tests under horizontal loads or on the shake table would be useful to investigate specifically their seismic behaviour. Finally, in order to improve both the effectiveness and the efficiency of the retrofitting works carried out on the built heritage within restoration and upgrade activities, numerical models and design criteria should be developed based on experimental results. As a first contribution, a simplified analytical approach based on limit analysis was used in this study that provides a reliable estimate of the load carrying capacity of the reinforced vault specimens, thus appearing suitable for expeditious assessment and preliminary design purposes.

## **ACKNOWLEDGEMENTS**

This work was carried out within the Research Projects “Composites with inorganic matrix for sustainable strengthening of architectural heritage” funded by the Italian Ministry for Foreign Affairs (Year 2017, Grant N. PGR00234) and “ReLUIS-DPC 2017, Thematic Area Innovative materials for interventions in seismic areas”, funded by the Italian Department of Civil Protection. Kerakoll SpA is also kindly acknowledged for cofounding this research and providing reinforcement materials.

## **REFERENCES**

- [1] Ochsendorf J. Guastavino Vaulting. The Art of Structural Tile. Princeton: Princeton Architectural Press, 2010.
- [2] Valluzzi MR, Modena C, de Felice G. Current practice and open issues in strengthening historical buildings with composites. Mater Struct 2014;47(12):1971-1985.

- [3] De Lorenzis L, Dimitri R, La Tegola A. Reduction of the lateral thrust of masonry arches and vaults with FRP composites. *Constr Build Mater*, 2007;21(7):1415-1430.
- [4] Valluzzi MR, Valdemarca M, Modena C. Behaviour of brick masonry vaults strengthened with FRP laminates. *J Compos Constr* 2001;5(3):163-169.
- [5] Foraboschi P. Strengthening of masonry arches with fiber-reinforced polymer strips. *J Compos Constr* 2004;8(3):191-202.
- [6] Borri A, Casadei P, Castori G, Hammond J. Strengthening of brick masonry arches with externally bonded steel reinforced composites. *J Compos Constr* 2009;13(6):468-475.
- [7] Borri A, Castori G, Corradi M. Intrados strengthening of brick masonry arches with composite materials. *Compos Part B-Eng* 2011;42(5):1164-1172.
- [8] Cescatti E, Da Porto F, Modena C. Analysis and comparison of EBR techniques applied on masonry vaults. *ACI SP*. To appear.
- [9] De Santis S, Carozzi FG, de Felice G, Poggi C. Test methods for Textile Reinforced Mortar systems. *Compos Part B-Eng* 2017;127:121-132.
- [10] Garmendia L, Larrinaga P, García D, Marcos I. Textile-Reinforced Mortar as strengthening material for masonry arches. *Int J Arch Her* 2014;8(5):627-648.
- [11] Ramaglia G, Lignola GP, Balsamo A, Prota A, Manfredi G. Seismic strengthening of masonry vaults with abutments using Textile Reinforced Mortar. *J Compos Constr* 2017;21(2):04016079.
- [12] Alecci V, Focacci F, Rovero L, Stipo G, De Stefano M. Extrados strengthening of brick masonry arches with PBO-FRCM composites: Experimental and analytical investigations. *Compos Struct* 2016;149:184-196.
- [13] Alecci V, Misseri G, Rovero L, Stipo G, De Stefano M, Feo L, Luciano R. Experimental investigation on masonry arches strengthened with PBO-FRCM composite. *Compos Part B-Eng* 2016;100:228-239.
- [14] D'Ambrisi A, Focacci F, Luciano R, Alecci V, De Stefano M. Carbon-FRCM materials for structural upgrade of masonry arch road bridges. *Compos Part B-Eng* 2015;75:355-366.
- [15] Castori G, Borri A, Corradi M. Behavior of thin masonry arches repaired using composite materials. *Compos Part B-Eng* 2016;87:311-321.
- [16] Girardello P, Pappas A, Da Porto F, Valluzzi MR. Experimental testing and numerical modelling of masonry vaults. In: *Proceedings of Int. Conf. on Rehabilitation and Restoration of Structures Chennai, India, 2013*.
- [17] Garmendia L, Larrinaga P, San-Mateos R, San-José JT. Strengthening masonry vaults with organic and inorganic composites: an experimental approach. *Mater Des* 2015;85:102-114.
- [18] De Santis S, Ceroni F, de Felice G, Fagone M, Ghiassi B, Kwiecień A, Lignola G., Morganti M, Santandrea M, Valluzzi MR, Viskovic A. Round Robin Test on tensile and bond behaviour of Steel Reinforced Grout systems. *Compos Part B-Eng* 2017;127:100-120.

- [19] Ascione L, de Felice G, De Santis S. A qualification method for externally bonded Fibre Reinforced Cementitious Matrix (FRCM) strengthening systems. *Compos Part B-Eng* 2015;78:497-506.
- [20] De Santis S, Napoli A, de Felice G, Realfonzo R. Strengthening of structures with Steel Reinforced Polymers: A state-of-the-art review. *Compos Part B-Eng* 2016;104:87-110.
- [21] de Felice G, Aiello MA, Bellini A, Ceroni F, De Santis S, Garbin E, Leone M, Lignola GP, Malena M, Mazzotti C, Panizza M, Valluzzi MR. Experimental characterization of composite-to-brick masonry shear bond. *Mater Struct* 2015;49(7):2581-2596.
- [22] de Felice G. Assessment of the load-carrying capacity of multi-span masonry arch bridges using fibre beam elements. *Eng Struct*, 2009;31(8):1634-1647.
- [23] De Santis S. Bond behaviour of Steel Reinforced Grout for the extrados strengthening of masonry vaults. *Constr Build Mater* 2017;150:367-382.
- [24] De Santis S, de Felice G. Steel reinforced grout systems for the strengthening of masonry. *Compos Struct* 2015;134:533-548.
- [25] Malena M, De Santis S, Pantò B, de Felice G. A closed-form analytical solution to the debonding of SRG on curved masonry substrate. *Key Eng Mater* 2017;747:313-318.
- [26] Blaber J, Adair B, Antoniou A. Ncorr: Open-Source 2D Digital Image Correlation Matlab Software. *Exp Mech* 2015;55(6):1105-1122.
- [27] De Canio G, de Felice G, De Santis S, Giocoli A, Mongelli M, Paolacci F, Roselli I. Passive 3D motion optical data in shaking table tests of a SRG-reinforced masonry wall. *Earthq Struct* 2016;10(1):53-71.
- [28] Tekieli M, De Santis S, de Felice G, Kwiecień A, Roscini F. Application of Digital Image Correlation to composite reinforcements testing. *Compos Struct* 2017;160:670-688.
- [29] Callaway P, Gilbert M, Smith CC. Influence of backfill on the capacity of masonry arch bridges. *Proceedings of the Institution of Civil Engineers: Bridge Engineering* 2012;165(3):147-158.
- [30] Pan B, Qian K, Xie H, Asundi A. Two-dimensional digital image correlation for in-plane displacement and strain measurement: a review. *Meas. Sci. Technol.* 2009;20(6):062001.
- [31] Caporale A, Feo L, Luciano R. Limit analysis of FRP strengthened masonry arches via nonlinear and linear programming. *Compos Part B-Eng* 2012;43(2):439-446.
- [32] Caporale A, Luciano R. Limit analysis of masonry arches with finite compressive strength and externally bonded reinforcement. *Compos Part B-Eng* 2012;43(8):3131-3145.
- [33] Caporale A, Feo L, Luciano R, Penna R. Numerical collapse load of multi-span masonry arch structures with FRP reinforcement. *Compos Part B-Eng* 2013;54(1):71-84.
- [34] Bernat-Maso E, Gil L, Marcé-Nogué J. The structural performance of arches made of few voussoirs with dry-joints. *Struct Eng Mech* 2012;44(6):775-799.

## FIGURE CAPTIONS

Figure 1. Side and top view of the experimental setup.

Figure 2. Construction of masonry vault specimens.

Figure 3. Ultra High Tensile Strength Steel (UHTSS) cord (a) and textiles with 8 cord/inch density (b) and 4 (c) cord/inch density.

Figure 4. Installation of the SRG reinforcement at the extrados of the vault.

Figure 5. Installation of the SRG reinforcement at the intrados of the vault.

Figure 6. Vertical displacements of bricks 10 and 17 (a), horizontal displacements of the abutments (b), out-of-plane displacements of the wood and Plexiglas panels (c), and vertical displacements of brick 17 and of the IPE240 beam (d) vs. time.

Figure 7. Load-displacement response curves.

Figure 8. Crack pattern and failure mode of UNR specimen.

Figure 9. Crack pattern, failure mode and strains in the textile of EX8 specimen.

Figure 10. Crack pattern, failure mode and strains in the textile for EX4 specimen.

Figure 11. Crack pattern, failure mode and strains in the textile for IN4 specimen.

Figure 12. Damage pattern surveyed after the test on EX8 (a-c), EX4 (d-f) and IN4 (g-i) vault specimens.

Figure 13. Deformed configurations of EX8 (a,b), EX4 (c,d) and IN4 (e,f) specimens compared to those of UNR at peak load (a,c,e) and at collapse (b,d,f).

Figure 14. Field of vertical displacements and arrows of total displacements at peak load in UNR (a), EX8 (b), EX4 (c) and IN4 (d) specimens. Arrows scaled by 2.

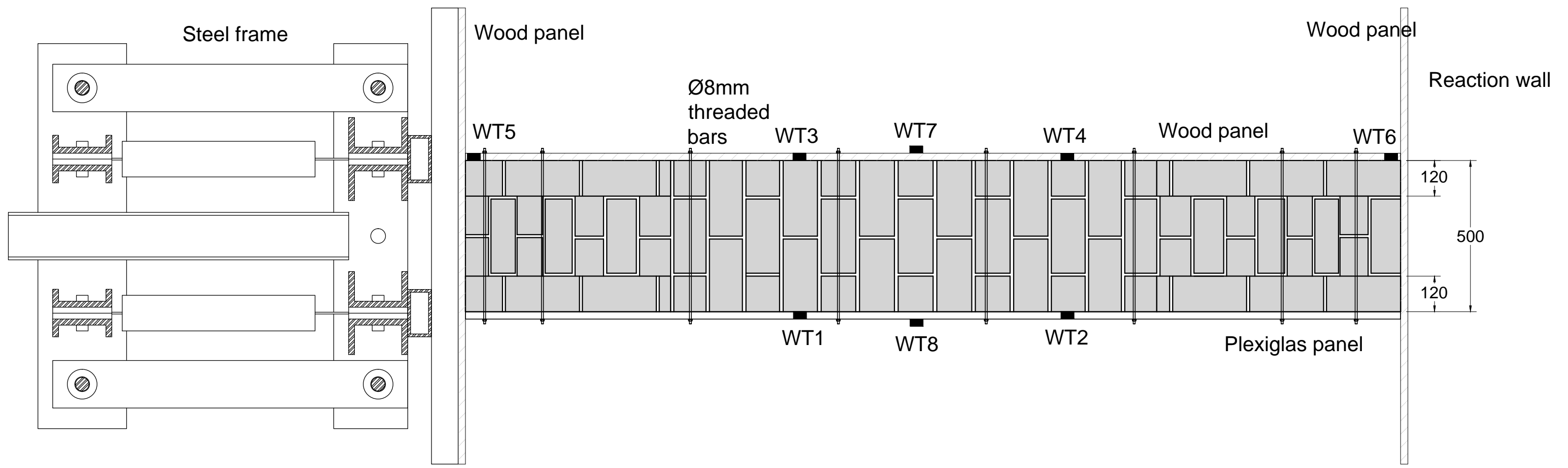
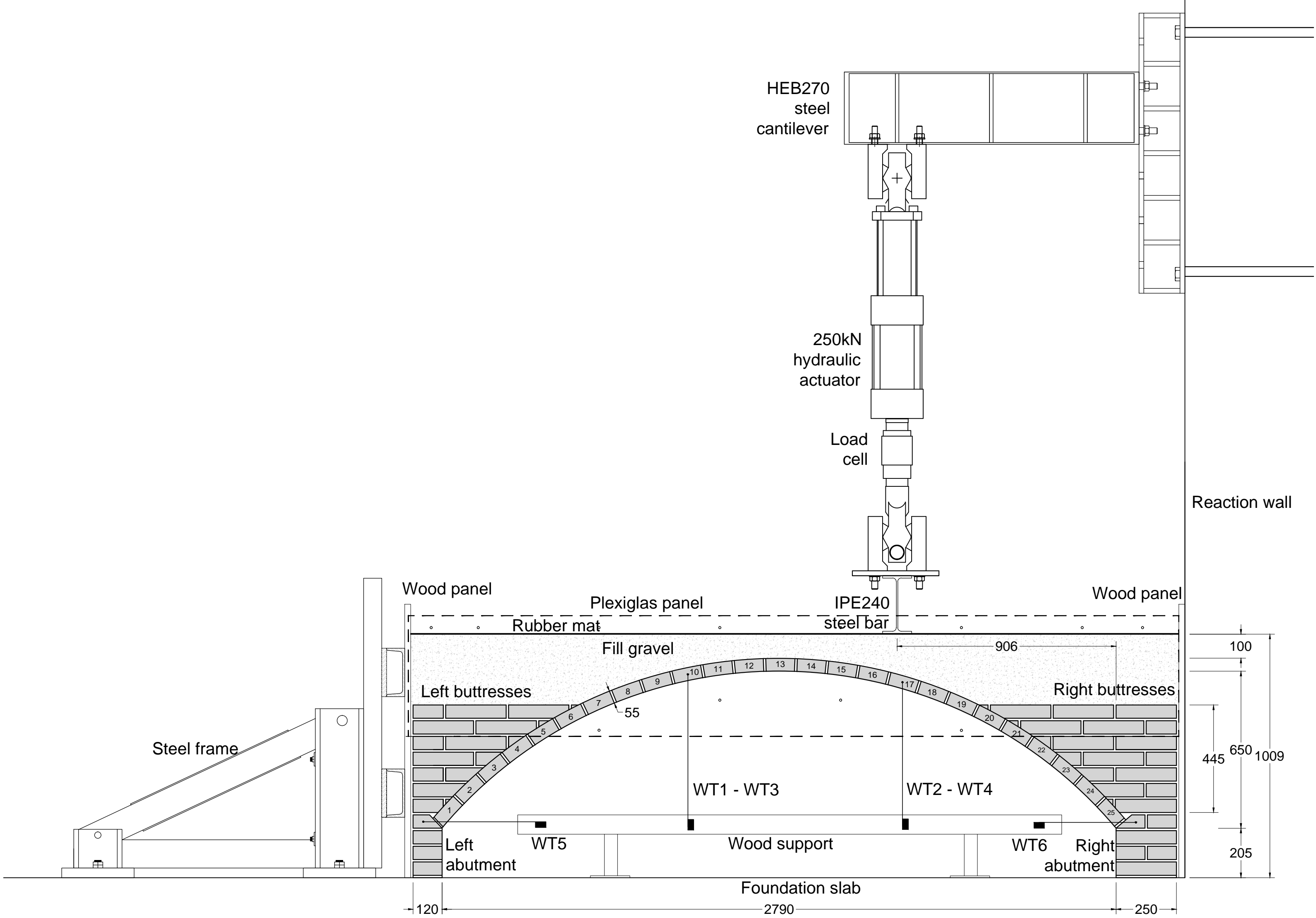
Figure 15. Field of vertical displacements and arrows of total displacements at collapse in UNR (a), EX8 (b), EX4 (c) and IN4 (d) specimens. Arrows scaled by 0.8.

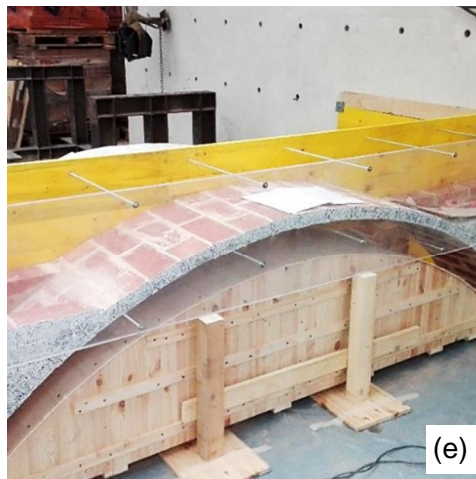
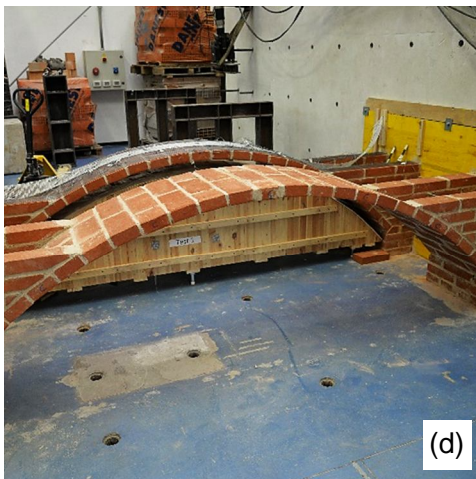
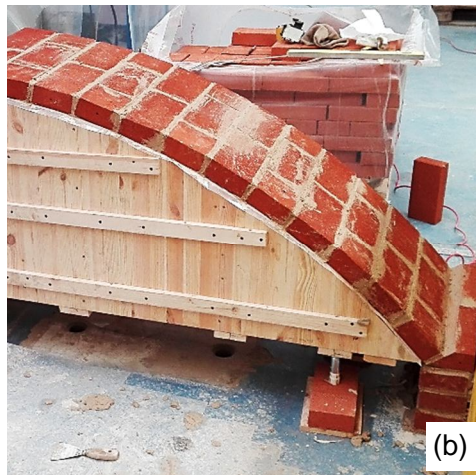
Figure 16. Collapse mechanisms of EX8 (a) and IN4 (b) specimens used for the analytical estimate of their load carrying capacity with limit analysis based approaches.

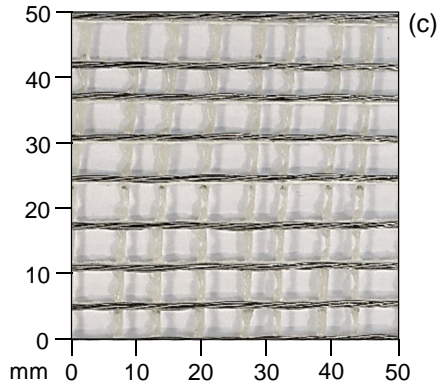
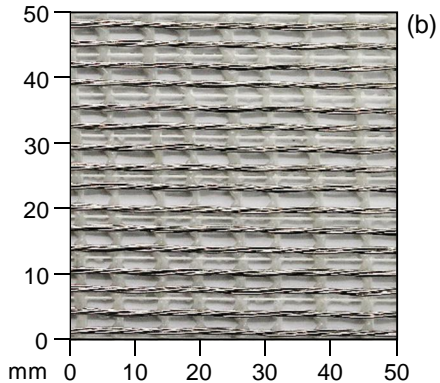
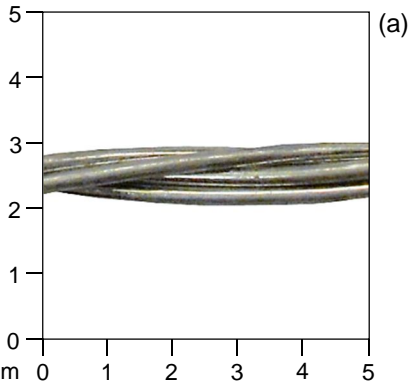
Figure 17. Axial load – bending moment strength domains of the cross section of the arch reinforced at the extrados (a) and at the intrados (b).

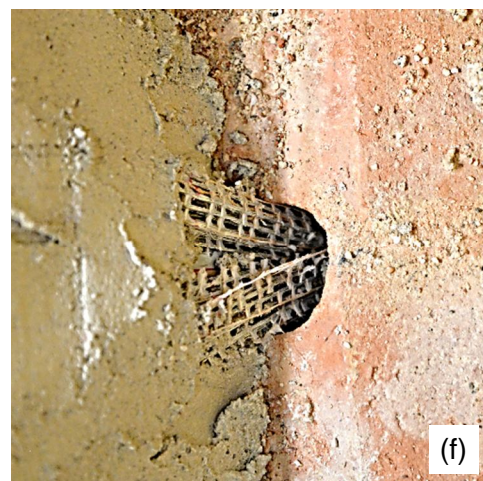
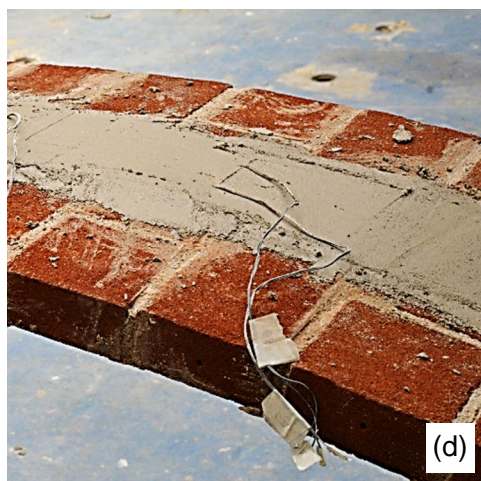
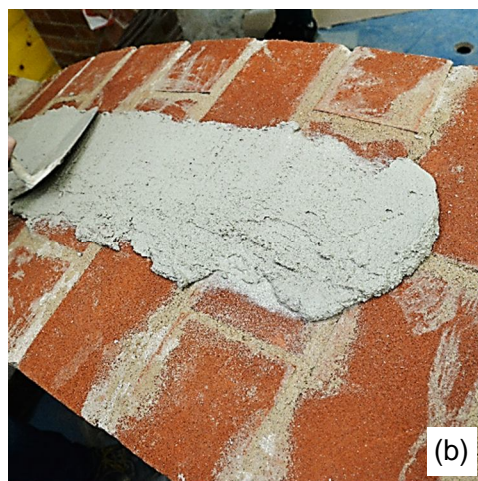
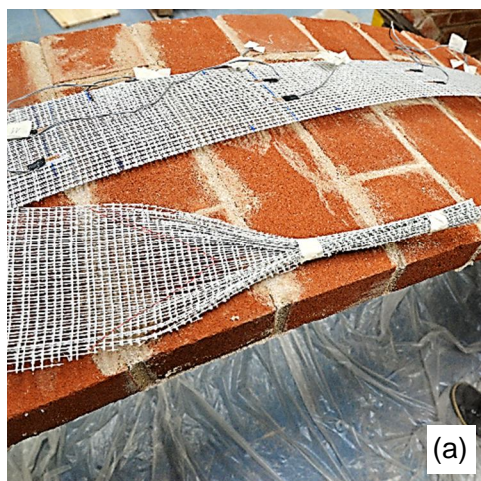
## TABLE CAPTIONS

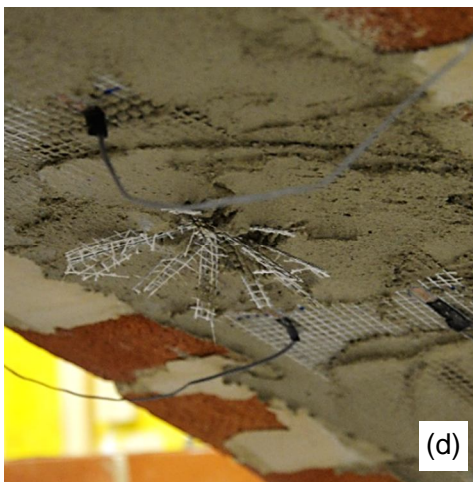
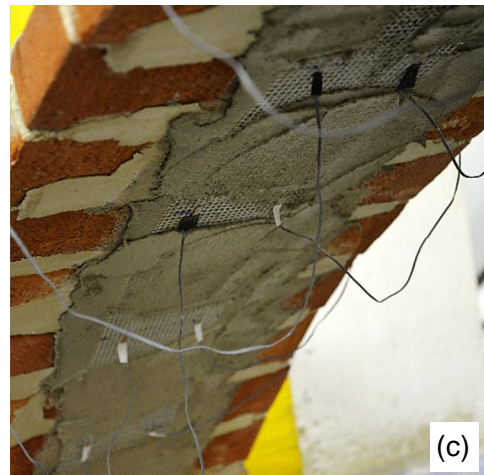
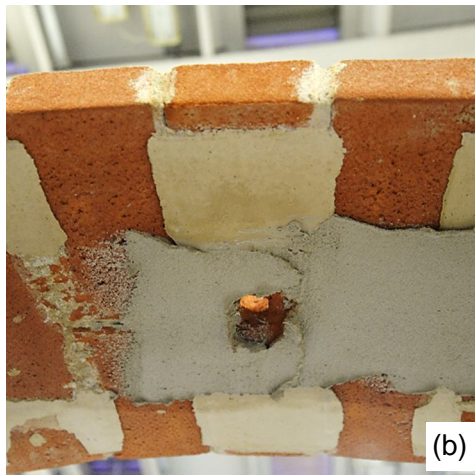
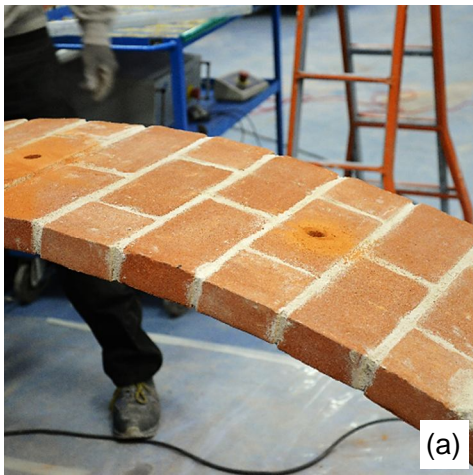
Table 1. Test results.

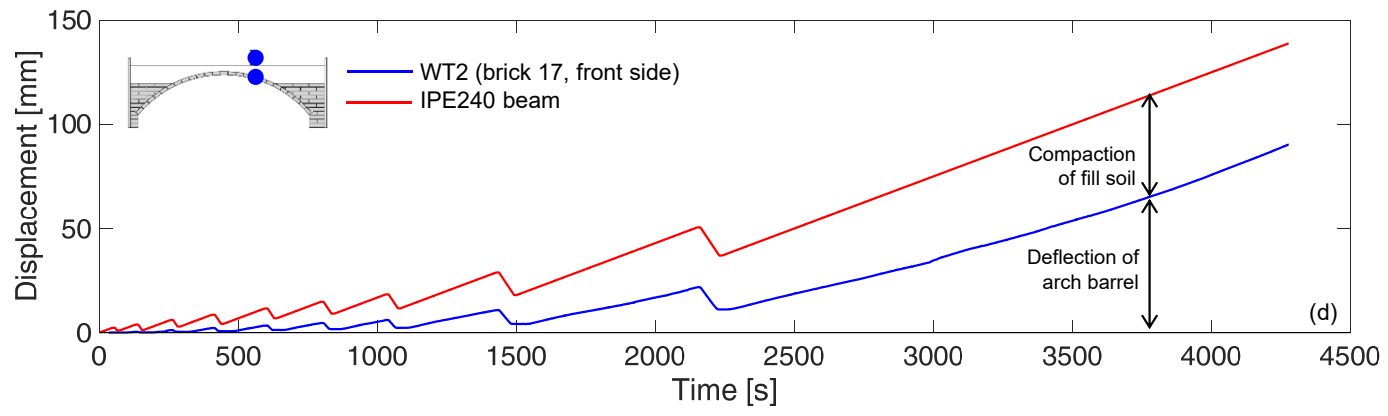
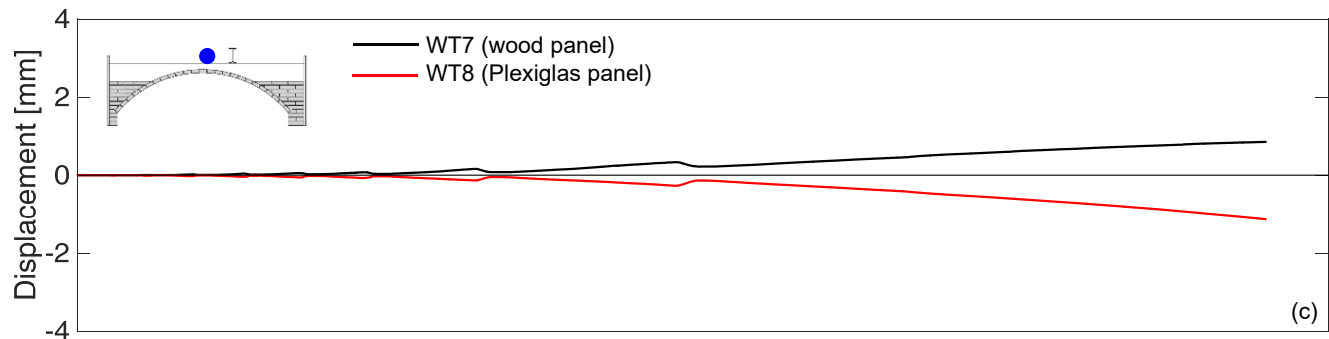
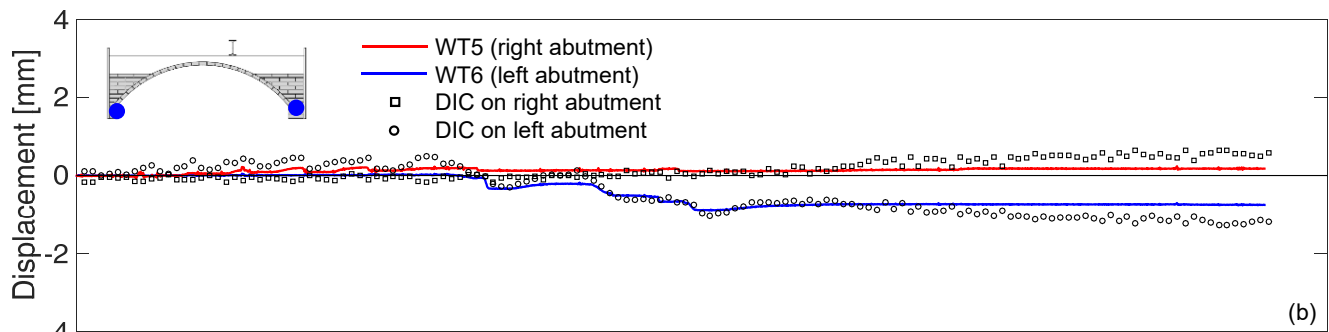
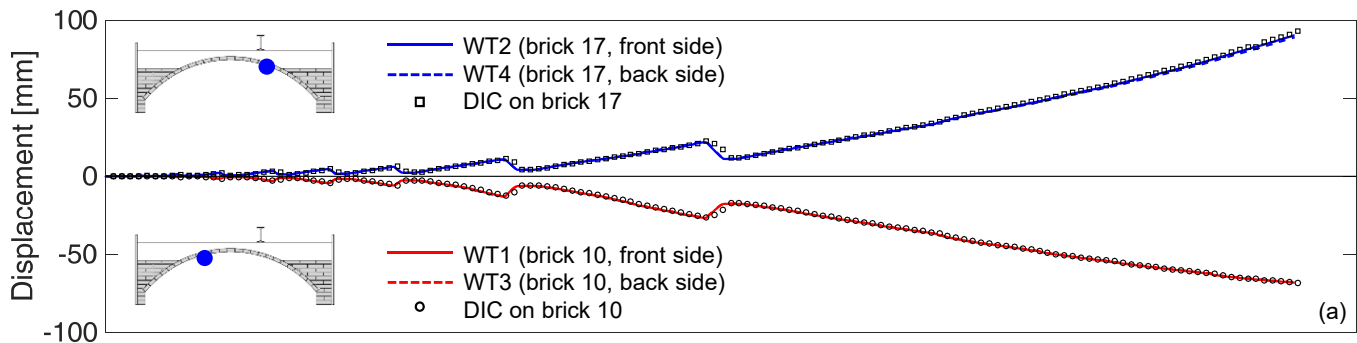


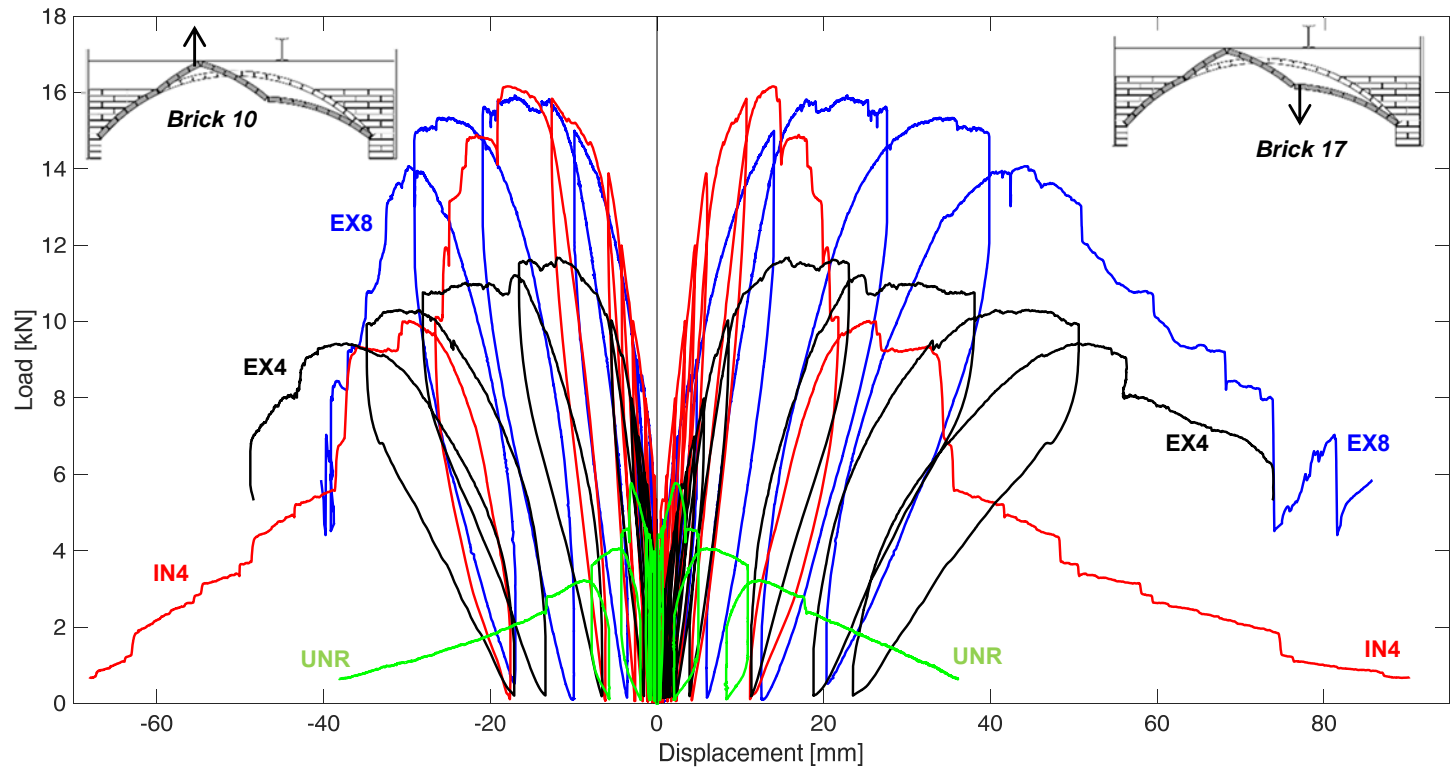


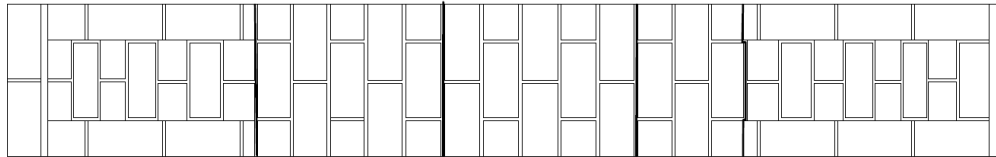
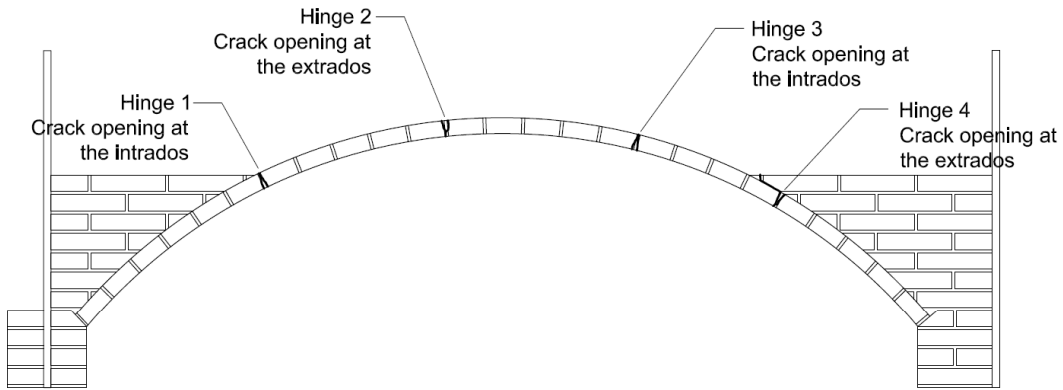


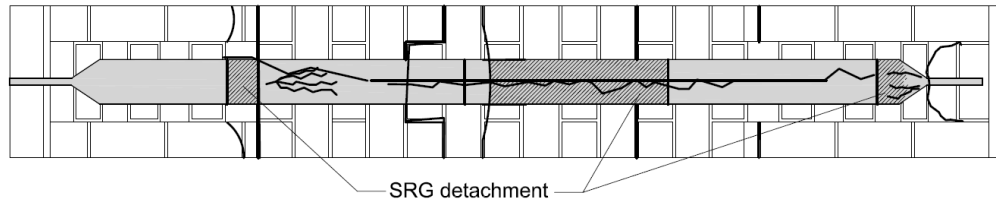
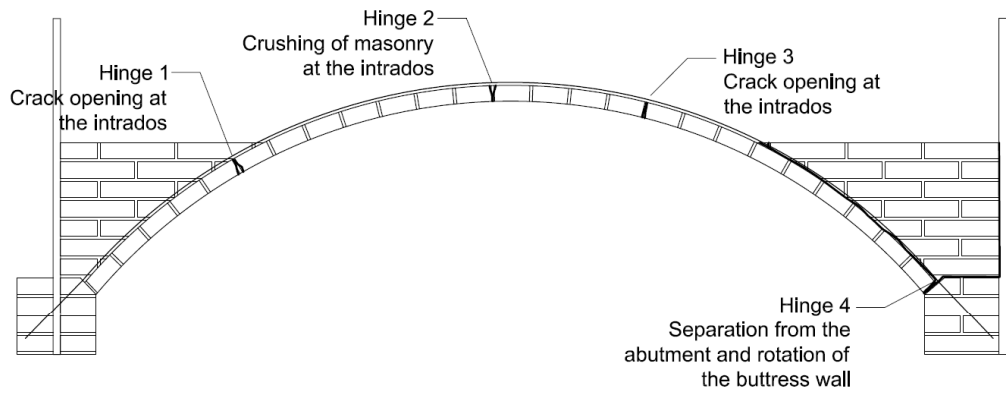




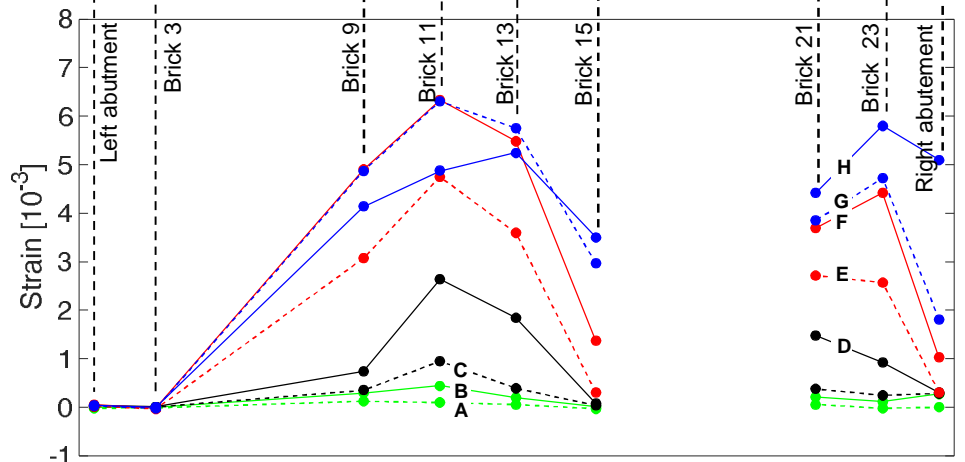
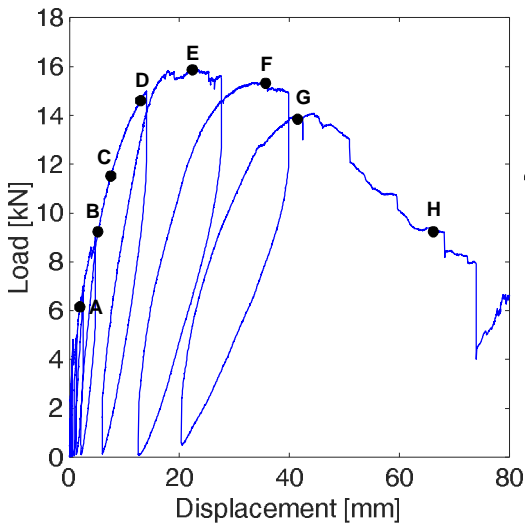


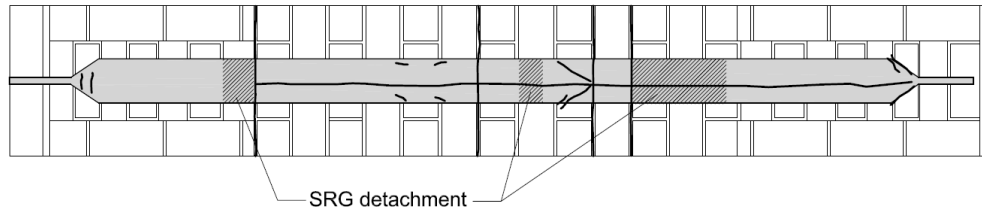
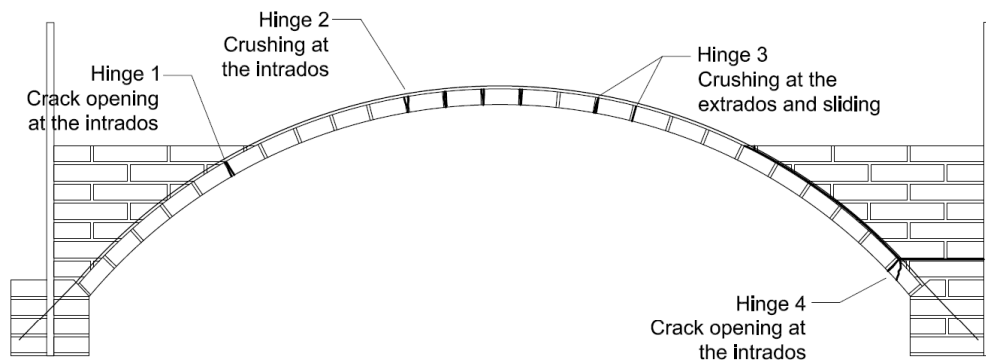




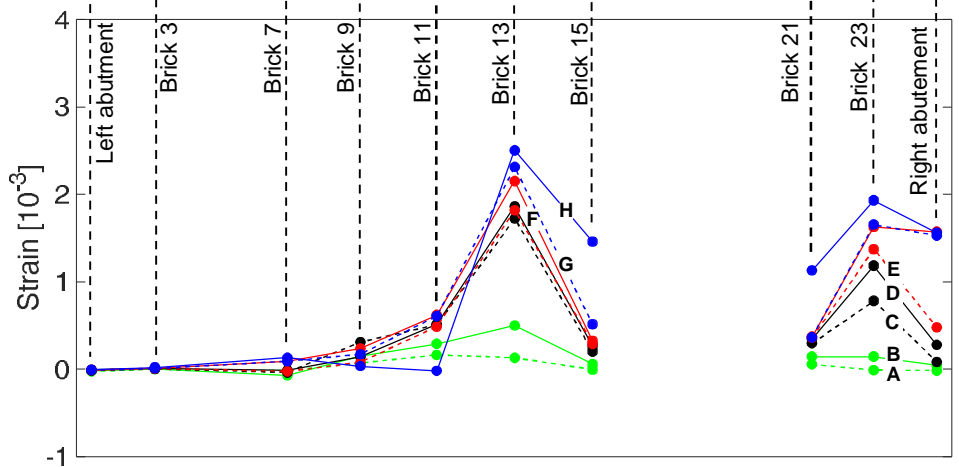
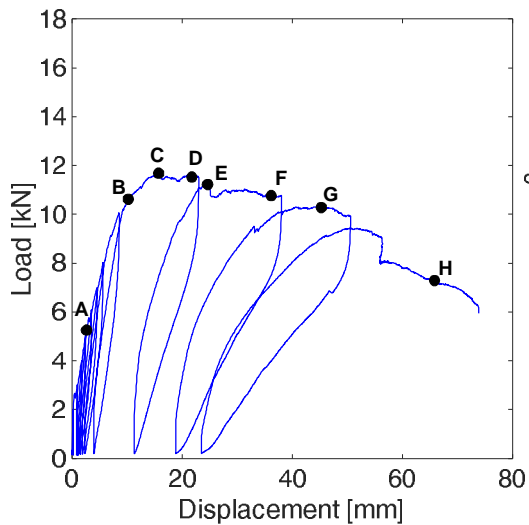


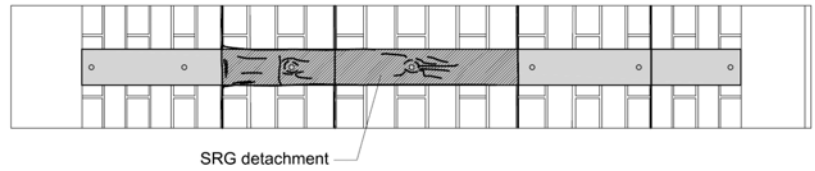
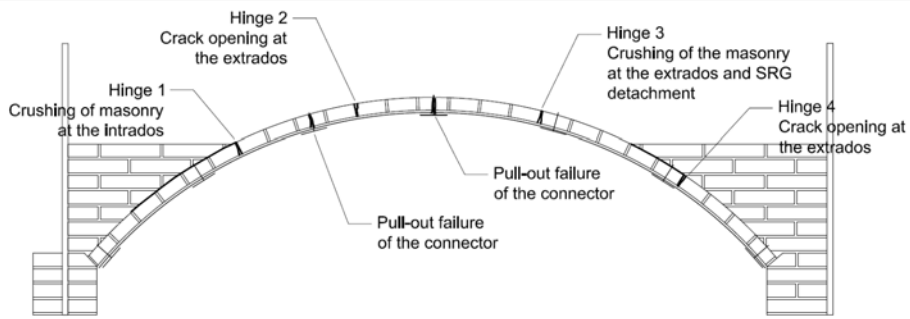
- Point A:  $s=1.9\text{mm}$   $F=5.8\text{kN}$
- Point B:  $s=5.2\text{mm}$   $F=9.2\text{kN}$
- -●- - Point C:  $s=7.5\text{mm}$   $F=11.5\text{kN}$
- Point D:  $s=12.9\text{mm}$   $F=14.5\text{kN}$
- -●- - Point E:  $s=22.8\text{mm}$   $F=15.9\text{kN}$
- Point F:  $s=35.6\text{mm}$   $F=15.3\text{kN}$
- -●- - Point G:  $s=41.5\text{mm}$   $F=13.8\text{kN}$
- Point H:  $s=66.1\text{mm}$   $F=9.2\text{kN}$



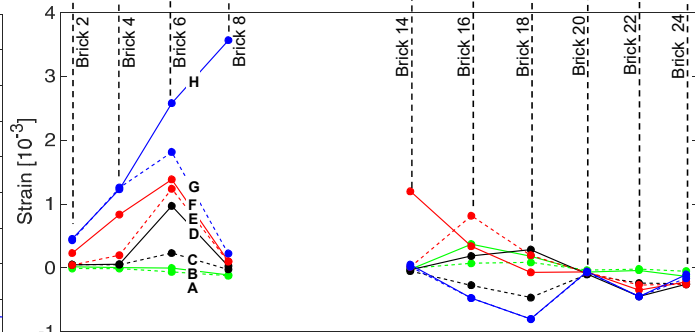
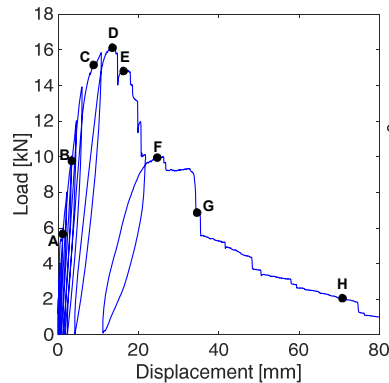


- Point A:  $s=2.6\text{mm}$   $F=5.8\text{kN}$
- Point B:  $s=7.6\text{mm}$   $F=8.3\text{kN}$
- -●- - Point C:  $s=15.8\text{mm}$   $F=11.7\text{kN}$
- Point D:  $s=21.8\text{mm}$   $F=11.5\text{kN}$
- -●- - Point E:  $s=24.5\text{mm}$   $F=11.2\text{kN}$
- Point F:  $s=36.1\text{mm}$   $F=10.7\text{kN}$
- -●- - Point G:  $s=45.2\text{mm}$   $F=10.3\text{kN}$
- Point H:  $s=65.8\text{mm}$   $F=7.3\text{kN}$

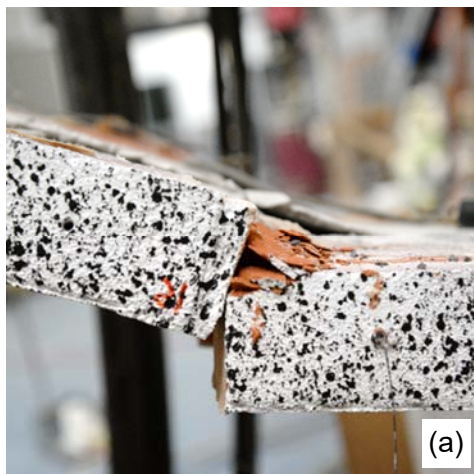




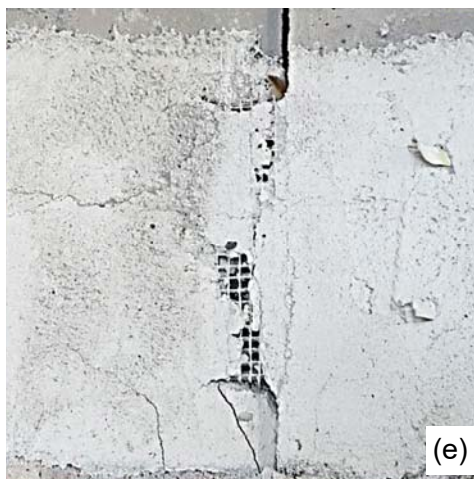
- Point A:  $s=1.4\text{mm}$   $F=5.8\text{kN}$
- Point B:  $s=3.5\text{mm}$   $F=9.8\text{kN}$
- Point C:  $s=8.9\text{mm}$   $F=15.2\text{kN}$
- Point D:  $s=13.9\text{mm}$   $F=16.2\text{kN}$
- Point E:  $s=16.3\text{mm}$   $F=14.8\text{kN}$
- Point F:  $s=24.7\text{mm}$   $F=9.9\text{kN}$
- Point G:  $s=34.6\text{mm}$   $F=6.9\text{kN}$
- Point H:  $s=70.8\text{mm}$   $F=2.0\text{kN}$



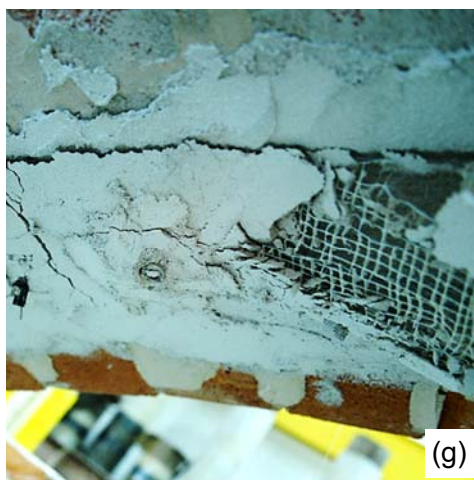
EX8

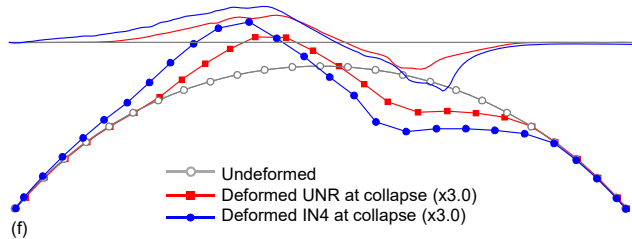
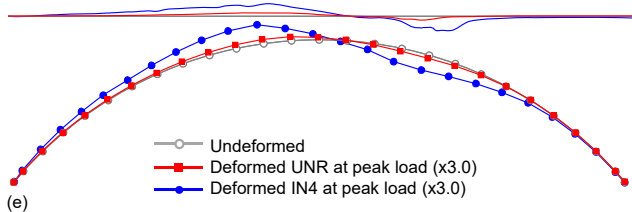
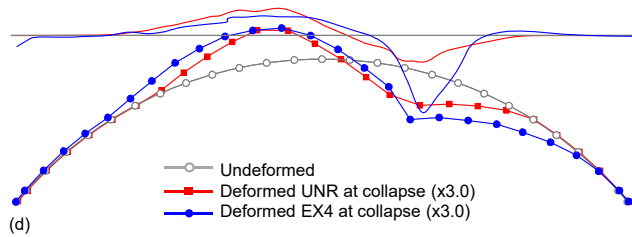
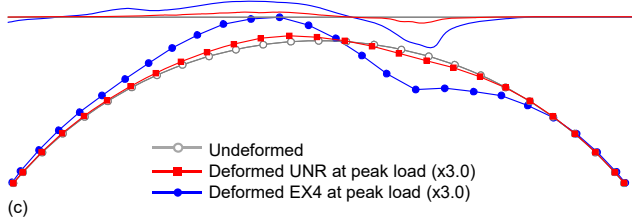
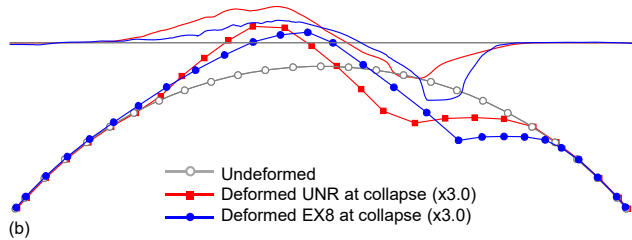
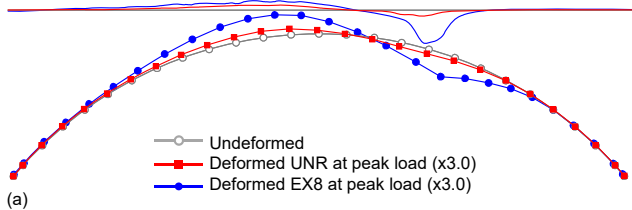


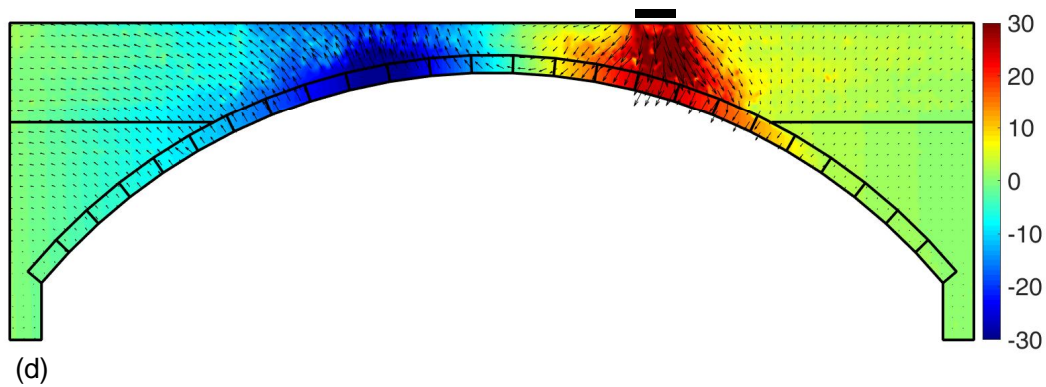
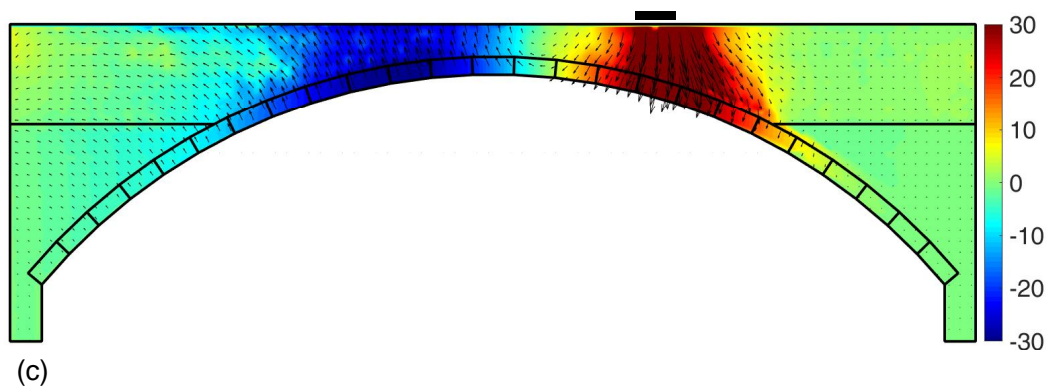
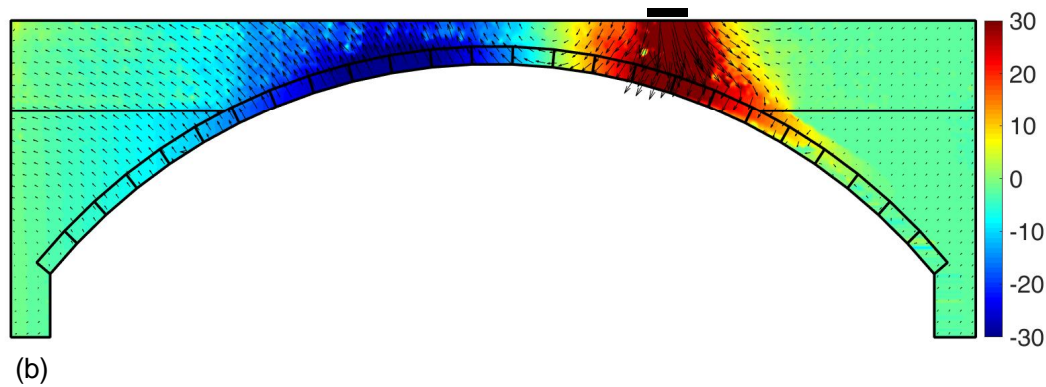
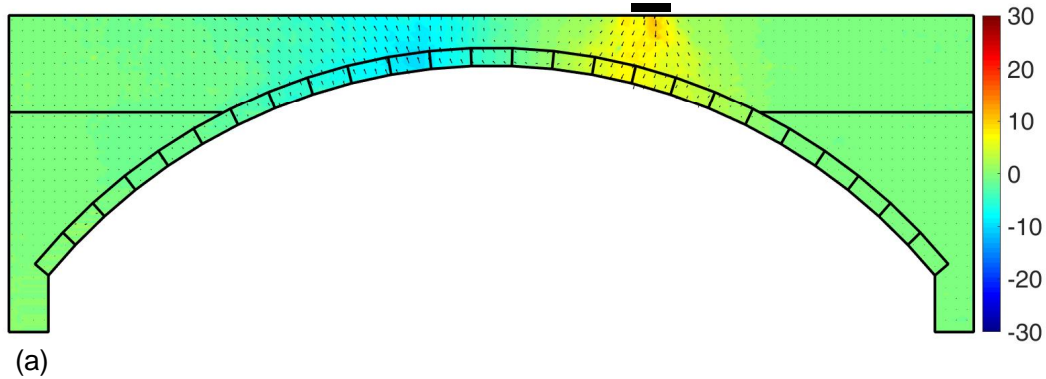
EX4

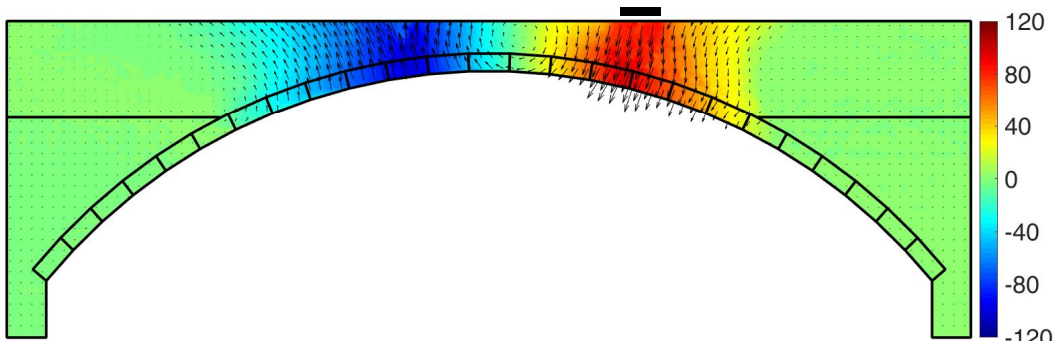


IN4

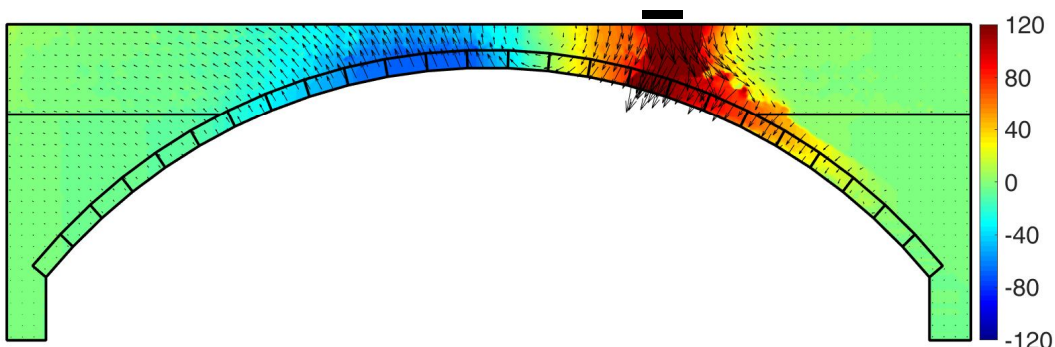




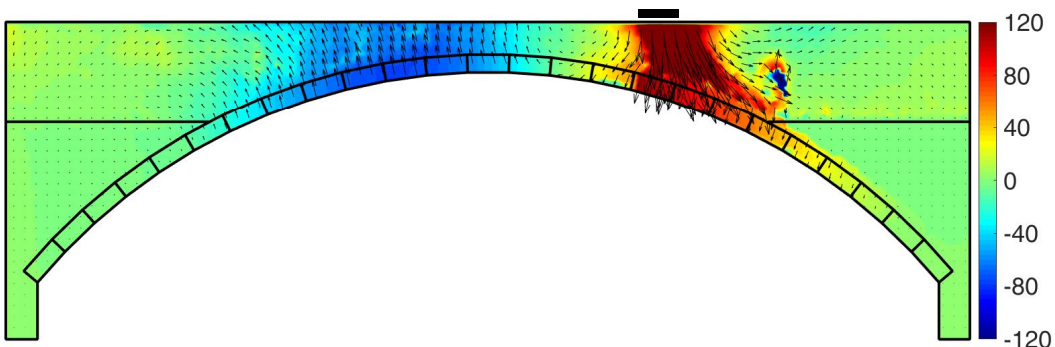




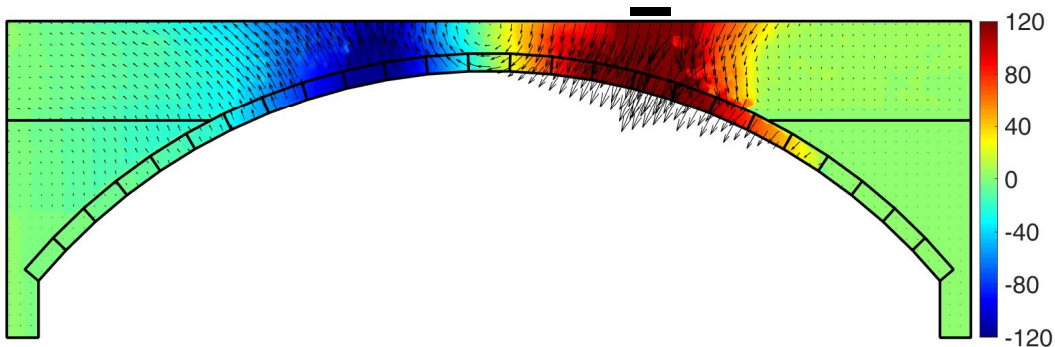
(a)



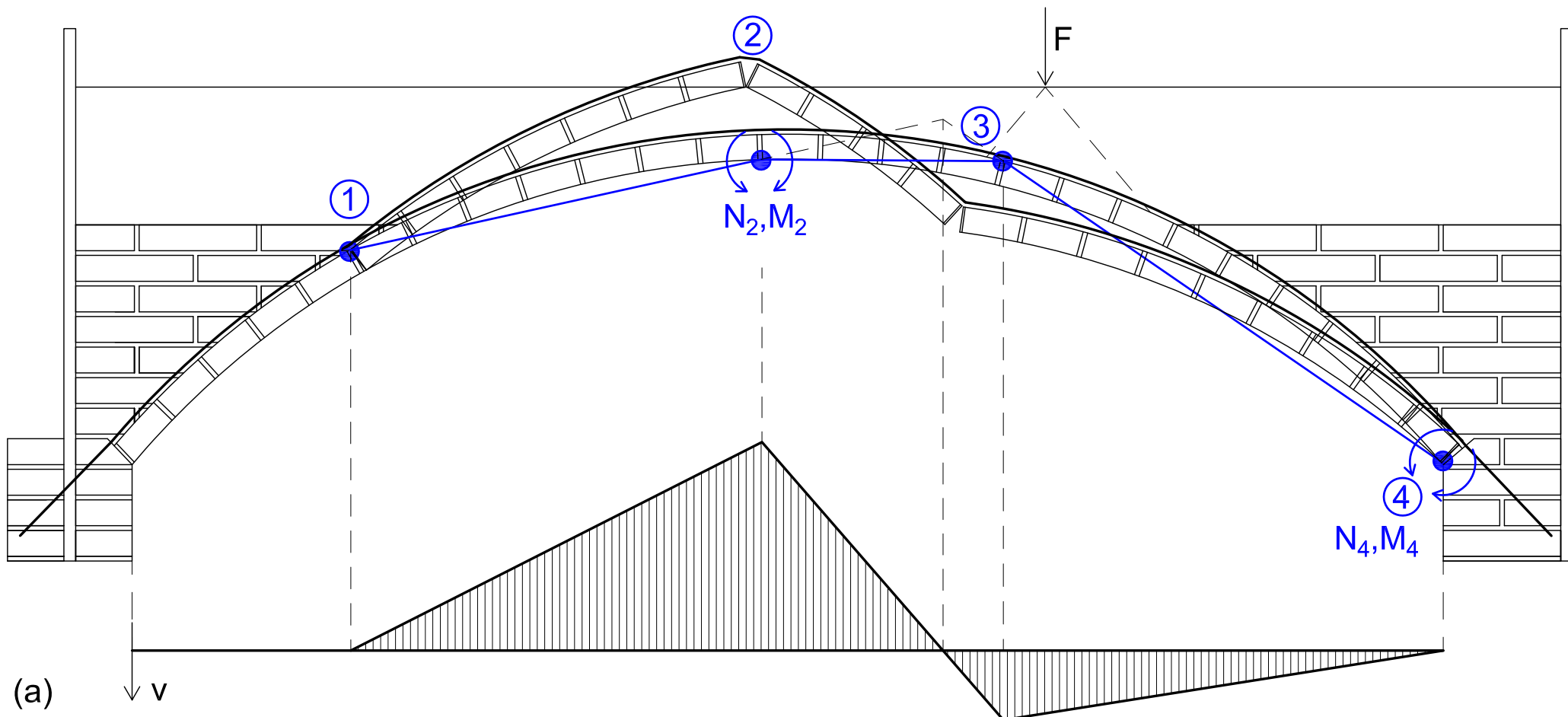
(b)



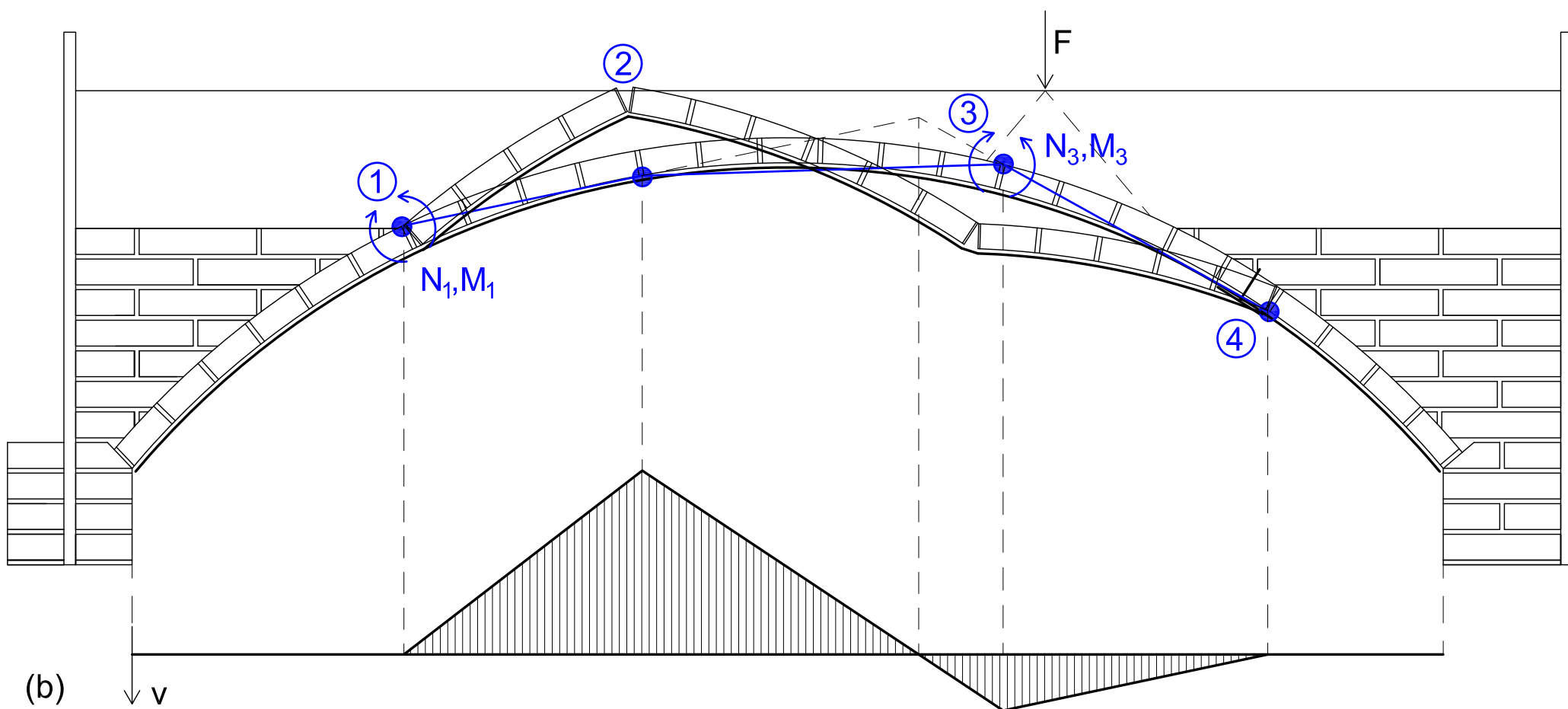
(c)



(d)



(a)



(b)

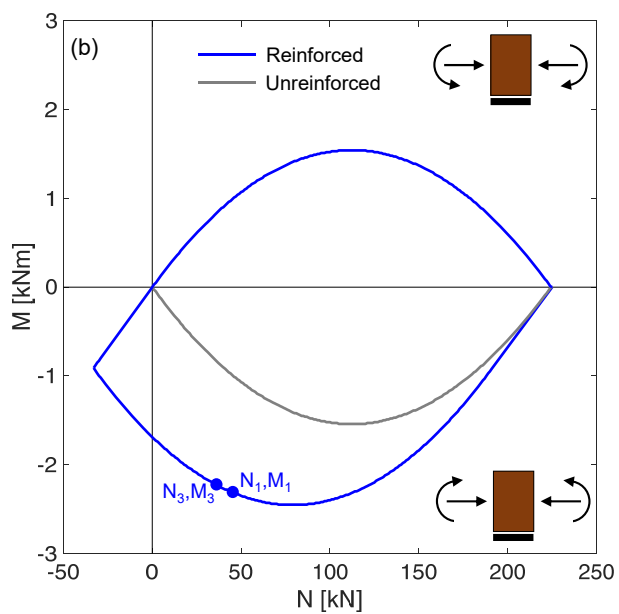
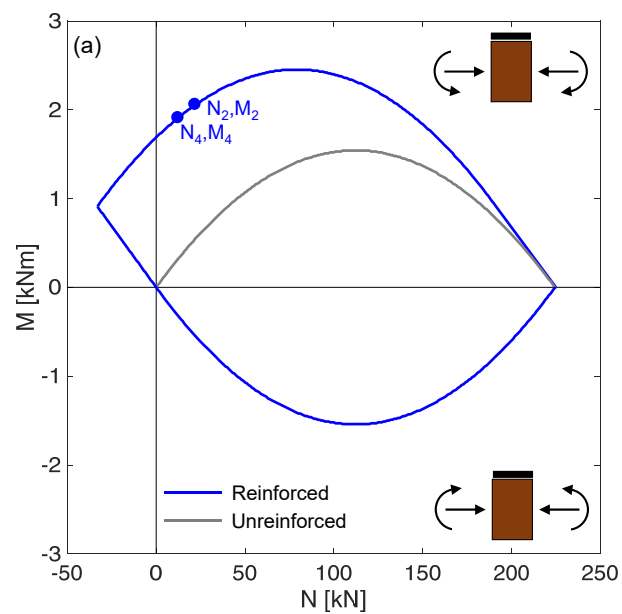


Table 1. Test results.

Specimen	$F_{\max}$ [kN]	$\Delta F_{\max}$ [-]	$s(F_{\max})^+$ [mm]	$s(F_{\max})^-$ [mm]	$s_u^+$ [mm]	$s_u^-$ [mm]	$\varepsilon_{\max}$ [-]	$\sigma_{\max}$ [N/mm <sup>2</sup> ]	$\eta_t$ [%]	$\eta_b$ [%]	Failure mode
UNR	5.8	–	2.2	–3.1	36.1	–38.1	–	–	–	–	Four hinge mechanism
EX8	15.9	2.74	22.8	–17.0	85.8	–40.3	$6.7 \times 10^{-3}$	1233	38.7	190.6	Crushing, SRG detachment, sliding
EX4	11.7	2.02	15.8	–12.0	73.9	–48.8	$2.5 \times 10^{-3}$	460	14.4	17.5	Sliding and crushing
IN4	16.2	2.79	13.9	–17.9	90.3	–68.1	$3.7 \times 10^{-3}$	681	21.4	25.9	SRG detachment, unfolding of connectors